Near-bed sediment transport during offshore bar migration in large-scale experiments

Florian Grossmann, David Hurther, Joep van Der Zanden, Iván Cáceres, Agustín Sánchez-arcilla, José Alsina

Near-bed sediment transport during offshore bar migration in large-scale experiments

Florian Grossmann,[1] David Hurther,[2] Joep van der Zanden,[3 4] Iván Cáceres,[1]

Agustín Sánchez-Arcilla,[1] José M. Alsina,[1]

Corresponding author: Florian Grossmann, Laboratory of Maritime Engineering, Department of Civil and Environmental Engineering, Universitat Politècnica de Catalunya, Barcelona, Spain. (florian.grossmann@upc.edu)

[1]Universitat Politècnica de Catalunya, Barcelona, Spain.

[2]Laboratory of Geophysical and Industrial Flows (LEGI), CNRS, Univ. Grenoble Alpes, Grenoble INP, France.

[3]Maritime Research Institute Netherlands, Wageningen, the Netherlands.

[4] Water Engineering and Management Department, University of Twente, Enschede, the Netherlands.

Abstract.

This paper presents novel insights into hydrodynamics and sediment fluxes in large-scale laboratory experiments with bichromatic wave groups on a relatively steep initial beach slope (1:15). An Acoustic Concentration and Velocity Profiler provided detailed information of velocity and sand concentration near the bed from shoaling up to the outer breaking zone including suspended sediment and sheet flow transport. The morphological evolution was characterized by offshore migration of the outer breaker bar. Decomposition of the total net transport revealed a balance of onshore-directed, short wave-related and offshore-directed, current-related net transport. The short wave-related transport mainly occurred as bedload over small vertical extents. It was linked to characteristic intrawave sheet flow layer expansions during short wave crests. The current-related transport rate featured lower maximum flux magnitudes but occurred over larger vertical extents. As a result, it was larger than the short wave-related transport rate in all but one cross-shore position, driving the bar's offshore migration. Net flux magnitudes of the infragravity component were comparatively low but played a non-negligible role for total net transport rate in certain cross-shore positions. Net infragravity flux profiles sometimes featured opposing directions over the vertical. The fluxes were linked to a standing infragravity wave pattern and to the correlation of the short wave envelope, controlling suspension, with the infragravity wave velocity.

Plain Language Summary

Nearshore sandbars are seabed features that protect coastal infrastructure behind many sandy beaches around the world. In response to waves they change in shape and distance to the beach. To improve understanding of their offshore movement, experiments representing natural conditions in a controlled laboratory setting were done. In this context, the underwater transport of sand was measured. The experiments featured groups of single short waves (less than 2.5 meters long), which transported sand in different ways. Single short waves largely transported sand towards the beach, and in a very thin layer close to the seabed. Currents, caused by the short waves and their breaking, largely transported sand away from the beach, and over a much wider layer. Interactions between the single short waves in a group created longer waves. They transported sand partly towards and partly away from the beach. The currents transported sand more effectively than the single short waves which explains the sandbar's offshore movement. The long waves transported less sand and only became important when transports from currents and short waves canceled each other out. This study provides useful information for better forecasting of sandbar movement, improving coastal protection.

1. Introduction

Beaches are natural barriers against the ocean wave action and inundation. Unlike classic man made flood protection structures, they are very dynamic systems which cycle through various states [*Wright and Short*, 1984]. Such morphological evolution must be understood in detail to harness their protective capabilities and services. In this context, bar offshore migration under erosive wave conditions is an important part of morphological evolution, as bars are important for wave energy dissipation and their morphodynamics must be considered in nourishment strategies for coastal protection.

Evidence from laboratory (e.g. *Eichentopf et al.* [2020]) and field experiments (e.g. *Mariño-Tapia et al.* [2007a]) suggests that bar offshore migration under erosive wave conditions is determined by wave breaking and the resultant hydrodynamics. In fact, several studies have confirmed a morphodynamic link between bar and wave breaking locations (e.g. *Plant et al.* [1999], *Pape et al.* [2010], *Alsina et al.* [2016] and *Eichentopf et al.* [2020]). This link was shown to result from the convergence of cross-shore sediment transport induced by wave breaking and from morphological feedback mechanisms (e.g. *Gallagher et al.* [1998] and *Mariño-Tapia et al.* [2007b]).

More specifically, bar migration depends on the net result of various sediment transport processes. *Gallagher et al.* [1998] highlighted the role of time-averaged offshore currents near the bed which lead to net offshore transport. The time-averaged offshore currents, on the other hand, originate from radiation stress gradients linked to wave breaking (e.g. *Svendsen* [1984]). Net onshore transport on the seaward side of breaker bars has often been linked to short wave asymmetry and skewness (e.g. *Hoefel and Elgar* [2003], *Henderson et al.* [2004] and *Brinkkemper et al.* [2018]). However, net onshore transport was calculated equally well with models that considered either process (e.g. *Hsu et al.* [2006] and *Fernández-Mora et al.* [2015]) and the numerical modeling of net onshore transport remains difficult [*van Rijn et al.*, 2011]. Another important factor may be infragravity wave-related net transports. However, these can be either onshore or offshore-directed and they importantly depend on the correlation of wave envelope and associated infragravity wave (e.g. *de Bakker et al.* [2016]).

The numerical assessment of sediment transport processes is based on parametrization, because the processes themselves often cannot be resolved (lack of computational capacity or physical understanding). Parametrization requires the use of calibration parameters and model performance was shown to heavily depend on them [*Dubarbier et al.*, 2015]). High quality calibration data sets facilitate parameter choice. However, such measurements are costly and difficult to obtain, especially under field conditions. In fact, modeling studies often rely on beach profile measurements of morphological evolution to gauge model performance (e.g. *Hoefel and Elgar* [2003], *Fernández-Mora et al.* [2015] or *Dubarbier et al.* [2015]). But the morphological evolution itself is only a product of sediment transport rates which depend on sediment concentration, flow velocity and their underlying processes.

Detailed measurements of sediment concentration and flow velocity may help to obtain a better understanding of processes. Optical Backscatter Sensors (OBS) are often used for measuring sediment concentration (e.g. *Alsina et al.* [2016] and *Brinkkemper et al.* [2018]). However, they only measure at one single location and they can only measure the relatively low concentrations typical in suspended load, neglecting bedload even though it can be highly important (e.g. *Fromant et al.* [2019] or *Mieras et al.* [2019]). Conductivity-based systems (*Ribberink and Al-Salem* [1992] and later *Lanckriet et al.* [2013]) were developed precisely for measuring high sediment concentrations very close to the undisturbed bed (bedload transport). Because the technology is based on conductivity, it struggles to capture suspended concentration and requires the combined use with other sensors, like OBS, to capture a sufficient part of the water column (e.g. *Mieras et al.* [2019]). Furthermore, both OBS and conductivity-based systems do not provide direct measurements of flow velocity to calculate sediment fluxes. The Acoustic Concentration and Velocity Profiler (ACVP; *Hurther et al.* [2011]), on the other hand, provides co-located profiles of concentration and velocity while covering suspended load [*van der Zanden et al.*, 2017a] and bedload at similar quality as conductivity-based systems [*Fromant et al.*, 2018]. In general, the measurement of sediment concentration and fluxes remains a very complex technological challenge subject to large uncertainties, especially in the evolving near-bed region where there are large vertical gradients.

Most of the studies with detailed measurements of sediment transport were conducted in the laboratory rather than the field (e.g. *O'Donoghue and Wright* [2004b], *van der Zanden et al.* [2017a], *Fromant et al.* [2019] or *Mieras et al.* [2019]). This is because detailed measurements often require very specific conditions in order to be successful (e.g. specific distance between sensor and bed), which can hardly be guaranteed in the field (e.g. changing water levels because of tides and bed evolution). However, laboratory experiments often fail to represent field conditions appropriately. Certain studies only consider monochromatic waves (e.g. *van der Zanden et al.* [2017a] and *Mieras et al.* [2019]), neglecting sediment transport from infragravity waves and leading to a very localized breaking region. The latter may result in higher undertow magnitudes and higher cross-shore gradients in sediment transport than expected under irregular waves. Another problem is the use of fixed, non-evolving beach profiles (e.g. *Mieras et al.* [2019]), neglecting the feedback mechanisms between hydrodynamics and morphology. Additionally, most studies fail to capture a sufficient number of cross-shore positions to observe the cross-shore evolution of processes and quantities (e.g. *Mieras et al.* [2019]).

In the present study, bichromatic erosive wave conditions (i.e. causing net offshore transport in most of the cross-shore beach profile) were used in a large-scale laboratory experiment with evolving beach profiles and state of the art instrumentation [*Hurther et al.*, 2011] in multiple cross-shore positions. This is expected to bridge the gap between the limited reproduction of field conditions in previous laboratory studies involving monochromatic waves and the limited detail of measurements in previous field studies, hence providing novel information on sediment transport processes and their relative importance for total net transport rate and morphologic evolution. Bichromatic waves are based on two primary frequency components and on their interaction during wave propagation (e.g. *Alsina et al.* [2016]). This produces realizations similar to random waves, while maintaining clear frequency signatures that facilitate spectral analysis and ensemble-averaging. They were shown to provide similar sediment transport rate and beach response as random waves, in contrast to monochromatic waves [*Baldock et al.*, 2011].

The paper is structured as follows: Sections 2 and 3 cover the experimental setup and data treatment. Section 4 summarizes results on morphological evolution and sediment transport within the sheet flow layer and above. Subsequently, the results are discussed and put into context with similar studies in section 5, followed by the main conclusions in section 6.

2. Experimental setup

2.1. Facility and test conditions

The present data were acquired within the HYDRALAB+ transnational access project "Influence of storm sequencing and beach recovery on sediment transport and beach resilience" (RESIST). The experiments were conducted in the large-scale CIEM wave flume at the Universitat Politcnica de Catalunya (UPC) in Barcelona. The flume is 100m long, 3m wide and 4.5m deep, and is equipped with a wedge-type wave paddle. The cross-shore coordinate x was defined as 0 at the wave paddle, increasing towards the beach (Figure 1a) and the still water depth was 2.5m. The vertical coordinate z was defined as pointing upwards from the still water level (SWL). The bed-referenced vertical coordinate ζ (Figure 1b) is the vertical elevation with respect to the time-dependent bed position (z_{bed}) – time dependent as erosion or accretion occurs during the experiments. The computation of ζ and z_{bed} will be explained in more detail in section 3.5.

The flume contained medium-grained sand with a median sediment diameter (D_{50}) of 0.25mm and a measured settling velocity w_s of 0.034m/s. A handmade slope of 1:15 was constructed as the initial profile before the start of the waves. Subsequently, a benchmark condition (B) of random waves with root-mean-square wave height H_{rms}=0.3m and peak period T_p=4s was applied over 30 minutes to homogenize and compact the manually shaped profile before the start of the actual experiments. The benchmark condition is performed to allow the experiments to start from the same initial profile ("benchmark") compacted by random waves. They were followed by erosive (E1 and E2) and accretive (A1, A2 and A3) wave conditions in three different sequences (Table 1). At intervals (30 minutes for some tests, including all featured E2 tests, and 60 minutes for other tests) the waves were paused to measure the beach profile, resulting in 4 to 6 tests per erosive wave condition and sequence (with a larger number of accretive tests because of the longer duration required for beach recovery). For additional details on the wave conditions, refer to *Eichentopf et al.* [2020].

The bichromatic erosive and accretive wave conditions consisted of two primary frequency components, yielding repeatable wave groups. This article focuses on the erosive wave condition E2, where $f_1 = 0.3041$Hz and $f_2 = 0.2365$Hz, because the complexity of processes under the accretive wave conditions merits separate analysis. Their wave group period (T_g) is defined as $T_g = \frac{1}{f1-f2} = 14.79$s and there were 3-4 short waves per group. Each one of the short waves is subject to a peak period of $T_p = 1/f_p = 3.7$s where $f_p = \frac{f_1+f_2}{2}$. The repetition period (T_r), i.e. the period after which a wave phase repeats exactly, was $T_r = 2 * T_g = 29.58$s. This resulted in time series composed of consecutive repeats of two slightly differing, alternating wave groups with seven short waves per T_r (a typical water surface elevation realization is sketched in blue in Figure 1a). In this study, T_r is of central importance because it determines the exact repetition of processes and the period for ensemble-averaging. At $H_1 = H_2 = 0.245$m the waves were fully modulated. They are classified "erosive" because their dimensionless sediment fall velocity $\Omega = \frac{H_{rms}}{T_p * w_s} = 2.54$ [*Wright and Short*, 1984]. The waves were generated based on first-order theory without active wave absorption. Previous studies described a minor influence of basin seiching when using, as was done in the present experiments, bichromatic waves with combination of primary frequencies far from the seiching modes and super–/subharmonics of the seiching modes (e.g. *Alsina et al.* [2016]). E2 produced the development of a breaker bar with successive offshore migration [*Eichentopf et al.*, 2020].

Not all of the tests with wave condition E2 are analyzed in depth in this study but only tests 36, 37, 39, 53, 54 and 105. In these tests measurements were taken on the offshore side of the outer bar. Data quality in concentration measurements on the onshore side of the outer bar crest was affected by wave breaking which induced undesired measurement gaps at specific phases within the periodically repeated wave sequence due to air bubble entrainment (see explanation in section 3.4).

2.2. Instrumentation

The experiments featured measurements of near-bed and outer flow velocities, sediment concentrations, water surface elevations and beach profiles. The primary measurements were taken from instruments deployed from a custom-built mobile frame (Figure 1b/c). The frame consisted of 30mm stainless steel tubing and was designed to minimize flow perturbations while withstanding wave impacts. It can be vertically adjusted with sub-mm accuracy and was re-positioned in between tests to measure hydrodynamics and sediment concentration in various locations surrounding the outer breaker bar. Additional measurements, mainly of water surface elevation, were taken in fixed locations all along the flume (Figure 1a).

The Acoustic Concentration and Velocity Profiler (ACVP; *Hurther et al.* [2011]) measured sediment concentrations, velocities and instantaneous bed elevations (because the seabed erodes and accretes during tests) below the mobile frame. The co-located sediment concentration and velocity measurements (cross-shore and vertical) are provided as vertical profiles of up to 20cm above the non-moving bed. Previous studies have shown the high precision of its measurements for bottom wave boundary layer studies (cf. *Chassagneux and Hurther* [2014]; *Fromant et al.* [2018]; *Fromant et al.* [2019]). In the current study, it was set to measure with a bin resolution of 1.5mm, a sampling frequency of 50Hz, horizontal radius of the sampling volume of about 3mm and an acoustic carrier frequency of 1MHz. While measuring, the ACVP tracks the instantaneous bed. In this way, it is possible to reference sediment concentration and velocity measurements to their instantaneous bed position.

Additional concentration measurements inside the ACVP measuring domain were obtained from a three-nozzle Transverse Suction System (TSS) on the mobile frame. It consisted of three vertically spread stainless-steel nozzles connected through plastic tubing to a peristaltic pump on top of the wave flume. Following *Bosman et al.* [1987], intake velocities amounted to 2.3m/s, exceeding the maximum orbital velocities measured by more than 1.5 to guarantee a constant sediment trapping efficiency. The nozzle intake diameter was 3mm (same as *Bosman et al.* [1987]) and the pump discharge was 1L/min. The 30mm long nozzles were oriented parallel to the bed and perpendicular to the wave direction. The nozzles were located in the lowermost 20cm above the bed at distances of 4cm, coinciding with the ACVP measurement domain (Figure 1b/c). The collected sediment-water mixture was treated following *van der Zanden et al.* [2017a] to obtain time-averaged concentrations. Above the ACVP measuring domain (approximately 25–30cm and 39-44cm above the instantaneous bed elevation), two Optical Backscatter Sensors (OBSs) were used to measure sediment concentrations at 40Hz. They were calibrated with sand samples from the wave flume in a replica of the apparatus explained by *Downing and Beach* [1989].

Outer flow velocities (i.e. higher than 10cm from the bed) were measured using a vertical array of three Nortek Vectrino Acoustic Doppler Velocimeters (ADVs; Figure 1b/c) on the mobile frame. The ADVs operated at an acoustic frequency of 10MHz and provided three component (cross-shore, longshore and vertical denoted u, v and w respectively) velocity measurements at 100Hz. The sampling volume is cylinder-shaped with 3mm radius and

2.8mm height. The lowermost ADV was located within the ACVP measuring domain, approximately 10–15cm above the instantaneous bed elevation. The other two mobile frame ADVs were located approximately 20–25cm and 30–35cm above the instantaneous bed elevation respectively.

Water surface elevations were measured at 40Hz using Resistive (wire) Wave Gauges (RWGs), Acoustic Wave Gauges (AWGs) and Pressure Transducers (PTs) in fixed locations along the flume (Figure 1). Additionally, one PT was attached to the mobile frame. PTs were deployed in the surf zone instead of RWGs because, especially in large-scale experiments, splashing water from breaking waves is known to affect data quality of RWG measurements negatively. The dynamic pressure measurements of PTs were converted to surface elevations via linear wave theory. The facility is equipped with a data acquisition system that combines steering of the wave paddle and time synchronization of instruments. ACVP and ADVs were recorded in separate computers and synchronized via trigger impulses from the facility's data acquisition system.

The active beach profile was measured in intervals of 30 minutes with a mechanical profiler. The measurements were conducted along the center line of the flume with a cross-shore resolution of 0.02m and a vertical measuring accuracy of 0.01m. During the experiments, the ACVP was continuously tracking the instantaneous bed elevation under the mobile frame.

3. Data analysis

3.1. Data cleaning

For each of the 30-minute tests, the first 5 minutes of data were discarded to remove potential transient hydrodynamic effects. In ADV measurements, a despiking routine based on *Goring and Nikora* [2002] was applied and spikes were not interpolated. Additionally, quality control measures were applied. Data with Signal to Noise Ratio (SNR) lower than 75% or the amplitude of the signal lower than 15dB were discarded. This led to removal of less than 5% of data. Custom-built data cleaning routines were applied to ACVP velocity measurements but did not affect output considerably. In the most onshore position considered (test 105), air bubbles were observed to penetrate into the ACVP measuring domain from above, affecting the measurements. The affected parts of the domain were not considered for analysis.

3.2. Data averaging

Continuous time series were separated into T_r ensembles based on water surface elevation measurements from offshore of the beach slope (at $x = 28.5$m). For the separation, the repetition period which produced the lowest standard deviation over all ensembles of the test, was applied consecutively throughout the measured time series to obtain ensembles. Subsequently, ensemble-averaging (indicated by angle brackets) at individual time steps t of a variable Ψ over N ensembles according to:

$$\langle\Psi\rangle(t) = \frac{1}{N}\sum_{n=1}^{N}\Psi(t+(n-1)T_r) \qquad (1)$$

was conducted. 46 ensembles were used for each test. For brevity the angle brackets and dependency on t will be omitted in most references to time-dependent, ensemble-averaged quantities. To obtain a higher resolution and to increase robustness, sediment concentrations and velocities were ensemble-averaged before applying detailed analyses to them (e.g. multiplying them to obtain sediment flux or time-averaging). Furthermore, ensemble-averaging isolates periodically–repeating processes from the stochastic variability inherent to concentrations and flow velocities, and allows more detailed study of the processes.

Time-averaging was conducted at wave group and short wave time scales. For the former, the whole repetition period T_r was considered as the averaging period T_{av}; for the latter, the repetition period was divided into single short waves, based on upcrossings of ensemble-averaged horizontal free stream velocity u_∞, taken at 5cm above the instantaneous bed elevation. Then, every intrawave time step during the repetition period was associated with one of the short waves and the averaging period T_{av} spanned from the first time step of a short wave to the last. Quantities like horizontal velocity u, for example, were then time-averaged according to:

$$\overline{u} = \frac{1}{T_{av}} \int_0^{T_{av}} \langle u(t) \rangle dt. \tag{2}$$

3.3. Exner transport calculations

To obtain net sediment transport rates from beach profile transect measurements, the beach profiles before and after each test were input into the Exner equation:

$$Q_p = Q(x_i) = Q(x_{i-1}) - (1-p) \int_{x_{i-1}}^{x_i} \frac{\Delta z}{\Delta t} dx \tag{3}$$

where $Q(x_i)$ is net sediment transport rate in the current cross-shore grid point, $Q(x_{i-1})$ is net sediment transport rate in the previous grid point, p is porosity of the sediment (measured to be 0.36), Δz is the elevation change calculated from beach profiles before and after the test and Δt is the duration of the test. To obtain output at every cross-shore grid point, a step-wise iteration starting from a known boundary condition is necessary. Very far offshore and on the emerged section of the beach only negligible transport rates are expected. This provides the necessary boundary conditions of zero net sediment transport rate. However, small measurement inaccuracies accumulate during the step-wise iteration over the beach profile. Therefore, the second boundary condition on the opposite end of the profile is commonly not satisfied and a residual remains. To account for the residual, it was evenly distributed over the whole cross-shore domain. In the process, the assumption that inaccuracies occur evenly over the whole profile, and not in single points, was made. For more details see *Baldock et al.* [2011].

3.4. Acoustic signal inversion to sediment concentration

The ACVP supplies profiles of acoustic backscatter intensity. Sediment concentration information can be derived from the ACVP backscatter intensities following the methodology of *Hurther et al.* [2011]. This inversion from intensity to concentration is done by iterating downwards from the emitter while accounting for the signal attenuation occurring along the way, as described in detail by *Fromant et al.* [2018]. The interpretation requires calibration of system-dependent, particle backscattering and attenuation constants.

In the present study two types of data were used for calibration and the same calibration constants were used in all tests. On the one hand, TSS measurements of time-averaged concentration were used to assess agreement in all considered tests. Here, a complicating factor was the time-varying elevation of TSS concentration measurements taken at a fixed vertical position over an eroding/accreting bed. In most tests the time-averaged concentration profile from the ACVP was within one order of magnitude of the single data points given by the TSS (comparative figures are not shown for brevity). On the other hand, volumetric net transport rates Q_p from beach profile transect measurements were used for calibration.

The ACVP domain is limited to 20cm above the bed with potential reductions due to bed elevation changes (as explained in detail in section 3.5). In offshore locations, the vast majority of sediment flux is found near the bed and within the ACVP domain. In onshore locations, however, fluxes occur at higher elevations above the bed as well. Therefore, additional net sediment transport rates at higher elevations from OBS and ADV measurements (explained in detail in section 3.6) were considered during the calibration. The results on net sediment transport rate (shown later in section 4.5) feature a comparison of the net transport rates obtained from the different methods to outline calibration agreement. Considering the fundamentally different methods of obtaining net transport rates and the uncertainties of the methods, the agreement is accepted as good enough.

During the calibration stage, dissatisfying net transport rate agreement became visible in tests on the onshore side of the bar crest. On the one hand, this may result from the limited vertical extent of ACVP and OBS/ADV measurements in combination with sediment suspension to higher elevations under breaking waves. On the other hand, detailed analysis of acoustic backscatter intensity profiles in the respective tests revealed signal drop-outs at crest phases of the largest short waves. The drop-outs are suspected to be caused by air bubbles which were entrained into the water column by breaking waves (see *Cáceres et al.* [2020]). The bubbles are suspected to block the signal entirely at those phases. Tests with drop-outs in more than 5% of the ensemble-averaged repetition period were discarded. In tests with successful concentration measurements, the upper limit of the sheet flow layer was obtained from the 8%-volumetric concentration criterion [*Dohmen-Janssen et al.*, 2001] applied to ensemble-averaged concentrations.

3.5. Bed elevation changes

The instantaneous bed elevation below the mobile frame was measured via the ACVP at every time step based on the methodology given in *Hurther and Thorne* [2011]. When considering bed evolution, two time-scales are important. On the one hand, there was gradual erosion and/or accretion over the duration of the whole test (blue line in Figure 2a). To ensure that measurements in different ensembles (e.g. from the start and end of a test) are comparable, the gradual trend of bed evolution over the test was obtained by lowpass-filtering the bed evolution (shown in red). Subsequently, every ensemble of instantaneous bed elevation, sediment concentration and velocity measurements was corrected for the gradual bed evolution, z_{filtered}, by shifting the ensembles' measurement bins vertically under the use of $\zeta_0(t) = z - z_{\text{filtered}}(t)$. In this way, all ensembles refer to the same intrawave coordinates instead of absolute coordinates and ensemble-averaging only occurs after the coordinate shift. Note, however, that referencing with the gradual trend of bed evolution limits the vertical extent of ensemble-averaged outputs to the smallest vertical extent over all ensembles (the ensemble-average at a specific elevation cannot be calculated when some of the ensembles do not feature output at this elevation). As a result, tests with large bed accretion under the ACVP only provide profiles with a very limited vertical extent.

On the other hand, there were instantaneous bed changes during the repetition period. Those were preserved and ensemble-averaged (after conversion to the vertically-shifted coordinate system) to obtain a detailed understanding of the intrawave bed evolution

(Figure 2b). In flow tunnel experiments (e.g. *O'Donoghue and Wright* [2004a]) the vertical coordinate system typically refers to the stillwater bed level. In the present study, the profile is evolving so that a different vertical reference is necessary. The bed level during the u_∞ upcrossing of the first short wave in the group, ζ_{cross}, was chosen for this purpose and the bed-referenced ζ-coordinate system (pointing upwards) is given by $\zeta(t) = \langle\zeta_0(t)\rangle - \zeta_{\mathrm{cross}}$. Whereas single instantaneous bed ensembles are limited to the ACVP's vertical resolution of 1.5mm (note the edginess in Figure 2a), their ensemble-average provides the bed elevation at sub-bin accuracy (Figure 2b). Yet, this ensemble-averaging makes the assumption that a large number of ensembles provides a more reliable output than the single bed elevation ensembles. An assumption justified by the fact that bed interfaces normally have a smaller extent than the available resolution of 1.5mm.

ACVP velocity and concentration filtering (explained in more detail in the following section), and time-averaging to obtain sediment flux profiles, was conducted under use of the ζ'-coordinate system to ensure that the signal is not interrupted by the evolving bed. The origin of the ζ'-coordinate system is the instantaneous erosion depth according to $\zeta'(t) = \zeta(t) - \zeta_{\mathrm{bed}}(t)$, where $\zeta_{\mathrm{bed}}(t)$ is the black line in Figure 2c/d , and the necessary additional coordinate shift was applied to already ensemble-averaged data. To illustrate why there is a need for the ζ-coordinate system, the Figures 2c/d feature an example of near-bed sediment concentration. The example shows considerable intrawave bed evolution during T_r (Figures 2c). In bins below the maximum intrawave bed elevation, the intrawave time series is intercepted by phases of no-flow boundary condition. This causes problems in filtering and phases of no-flow boundary condition should not influence the value of outputs over the whole time series – neither outputs from filtering nor from time-averaging. Use of the ζ'-coordinate system ensures that time-averaging over T_r does not consider values from no-flow boundary conditions and that reliable outputs are obtained from filtering. Nevertheless, to appreciate bed elevation changes during T_r, filtered intrawave time series will be shifted back to the ζ-coordinate system for graphical representation.

3.6. Sediment transport calculations

Sediment fluxes, q, from ACVP measurements were calculated as the product of co-located horizontal velocity and sediment concentration. To obtain a better understanding of sediment transport processes, a Reynolds decomposition was applied to ensemble-averaged concentrations and velocities:

$$q_{tot} = \langle u \rangle \langle C \rangle = \overline{u}\overline{C} + u_{ig}C_{ig} + u_{sw}C_{sw} \tag{4}$$

where subscript "ig" indicates infragravity components and subscript "sw" indicates short wave components. In data treatment, the fluctuating contributions are separated into frequency bands via filtering. Note that in the present study the short wave component does not contain fluctuations at turbulence frequencies because of prior ensemble-averaging. In the multiplication of decomposed concentrations and velocities only the highly correlated terms are considered, assuming that the other terms are negligibly low (e.g. *Ruessink et al.* [1998] or *Brinkkemper et al.* [2018]). In fact, the net transport rates from those terms were verified to be multiple orders of magnitude lower than the considered ones (not shown for brevity).

Fourier-based filtering techniques require a certain length of the time series in order to capture all harmonic components correctly. Therefore, the ensemble-averages of concentration and velocity were artificially repeated a number of times (>50) before applying a 6^{th} order Butterworth filter with cut-off frequency 0.117Hz. Note that the cut-off frequency was optimized via spectral analysis to ensure the clean separation of frequency bands. The high-passed outputs were multiplied to obtain short wave sediment fluxes, q_{sw}. In the low-passed outputs, the time-average was subtracted and they were then multiplied to obtain infragravity sediment fluxes, q_{ig}. Net fluxes were then obtained by time-averaging the time dependent fluxes as explained previously (section 3.2).

The net current-related (mean) flux, q_c, was obtained by time-averaging total concentration and velocity and multiplying them. Net sediment transport rates from ACVP measurements, Q_{ACVP}, were obtained by depth-integrating ensemble-averaged sediment fluxes at every time step of T_r and averaging over time at wave group and short wave scales. In offshore positions, the ACVP measuring domain is expected to encompass all notable sediment flux. Closer to the outer bar crest, sediment is suspended to higher elevations so that sediment fluxes also occur outside the ACVP domain.

Therefore, additional net fluxes and transport rates were calculated from OBS and ADV measurements. Due to bed elevation changes over the test (Figure 2a), the instruments measured at different elevations over the bed. At the used ADV vertical elevations, small vertical gradients in the velocity profile are expected. The concentration profiles, on the other hand, may feature large vertical gradients. Therefore, every concentration measurement from OBS was first associated with its elevation over the instantaneous bed in the ζ'-coordinate system. Second, the measurements were grouped in bins of 5cm vertical elevation. Finally, at every intrawave phase the ensemble-average was taken over the measurements within each group, outputting a single data point for every 5cm vertical bin. Spline and logarithmic functions were then fitted to the data points from OBS and ADV measurements respectively. Subsequently, the fitted functions were evaluated in elevations below the highest ADV data point. As the highest ADV data point was always located below the highest OBS data point (Figure 1), there was no extrapolation of data. Subsequently, decomposition and calculation of sediment fluxes from OBS and ADV were done in the same way as described previously for fluxes from the ACVP.

For total net sediment transport rates, depth-integrals were calculated at every time step of T_r over the total vertical domain available from ACVP, OBS and ADV. For bedload net transport rates, instantaneous erosion depths and upper sheet flow limits were used as integration boundaries (within the ACVP measuring domain). For suspended load net transport rates, upper sheet flow limits and the upper ends of the domain available from ACVP, OBS and ADV were used as integration boundaries.

3.7. Cross-shore data aggregation

In most analysis steps, results from different tests and different E2 sequences will be aggregated to obtain a cross-shore resolution of measurements around the migrating outer breaker bar. To do so, the cross-shore positions of measurements were normalized with the breaker bar cross-shore position based on visually-identified bar crests, as exemplified in Figure 3 via the dashed vertical lines. The validity of this normalization for the study of morphodynamic processes was shown in earlier studies (e.g. *Mariño-Tapia et al.* [2007a] and *Eichentopf et al.* [2018]). To confirm this for the present data, Figure 4a shows that relative, rather than absolute, cross-shore coordinates determined bed evolution (cf.

Eichentopf et al. [2018], Figure 9 and following their calculation procedure). Additionally, Figure 4b shows that profiles in the considered tests had a very similar shape in the vicinity of the outer bar crest (3.5m offshore and onshore of it; note the relative cross-shore coordinate $x' = x - x_{bar}$) and that bars had similar heights.

4. Results

4.1. Morphological evolution

Figure 3 exemplifies the morphological changes occurring over successive E2 tests within sequence 2. Application of wave condition B already led to formation of a small outer bar, as can be observed from the differences between the initial, handmade profile and the profile before test 53. Under erosive wave condition E2, the outer bar is observed to take a distinct shape and migrate offshore while slightly changing in shape and distance to SWL (65m $< x <$ 67.5m). Similarly, an inner bar grows and migrates offshore (67.5m $< x <$ 70m). There are bar troughs onshore of both bars. The inner surf zone and the shoreline erode and retreat. The described morphological evolution was observed in all tests with wave condition E2, see [*Eichentopf et al.*, 2019] for a detailed description of profile evolution.

4.2. Hydrodynamics

Figure 3 displays the cross-shore evolution of water surface elevation quantities. To obtain the wave heights of short waves, $H_{rms,sw}$, and infragravity (long) waves, $H_{rms,ig}$, the power spectrum of water surface elevation was integrated over their respective frequency bands using the cut-off frequency 0.117Hz (same frequency as used for separation of concentration and velocity (section 3.6)). The cross-shore evolution of $H_{rms,sw}$ indicates the dissipation of energy at short wave frequencies through wave breaking, which also affects the size of the short wave orbits and, therefore, η_{max} and η_{min}. The cross-shore evolution of $H_{rms,ig}$ shows distinct minima and maxima. In experiments with similar bichromatic waves in the same wave flume, *Alsina et al.* [2016] attributed such a distinct $H_{rms,ig}$ cross-shore structure to infragravity wave reflection at the beach and breakpoint-generation of infragravity waves (see *Moura and Baldock* [2017] and *Padilla and Alsina* [2018]). Furthermore, $H_{rms,ig}$ is larger than $H_{rms,sw}$ close to the shoreline, consistent with short wave breaking and energy dissipation. In agreement with expectations under breaking waves, time-averaged water surface elevations, $\overline{\eta}$, indicate a set-down offshore of the visually-identified breakpoints and a set-up onshore of them.

Figure 5 shows measurements from the mobile frame of time-averaged (mean) velocities in their cross-shore positions relative to the bar crest. Note that the figure aggregates data from all E2 tests with successful sediment concentration measurements and, therefore, features an ensemble-averaged beach profile centered at the bar crest, as illustrated in Figure 4b. In contrast to the mechanical profiler, the ACVP considers instantaneous bed evolution. The length of its ensemble-averaged measuring domain is limited by the smallest distance between emitter and bed which occurred over the whole test (section 3.5) and more accretion was observed in the tests on the seaward face of the bar crests (seaward bar migration). This led to the shorter ACVP domain visible.

Good agreement between ACVP and ADV time-averaged velocity measurements becomes visible (Figure 5a). Only at cross-shore locations close to the bar crest there are small discrepancies. Those may result either from differential appreciation of breaking processes due to the different configuration of the instruments or from the fact that time-averaging of ACVP measurements is always done at the same elevation relative to the bed, whereas time-averaging of ADV measurements is always done at the same absolute elevation. The largest depth-dependent magnitudes of time-averaged velocity are observed just offshore of the bar crest (Figure 5b). In the furthest offshore location (test 36, 2.4m offshore of bar crest), time-averaged onshore velocity becomes visible close to the bed. This may result from short wave streaming [*Longuet-Higgins*, 1953]. Closer to the bar crest, the wave breaking influence and return current, or undertow, is more evident.

4.3. Intrawave hydrodynamics and sediment dynamics

4.3.1. Shoaling region

Figure 6 presents ensemble-averaged measurements resolving T_r in a single test 2.4m offshore of the bar crest. During T_r, seven short waves (numbered in Figure 6b) occur. As mentioned previously (section 3.2) and visible in Figure 6, the delimitation into short waves was based on upcrossings of $\langle u_\infty \rangle$. T_r is made up of two wave groups with period 14.79s so that $T_r = 2 * T_g = 29.58$s. Ensemble-averaged intrawave η-measurements over T_r (Figure 6a) show larger amplitudes of the short waves compared to the associated infragravity wave (shown in light blue). As expected under two wave groups, two crests ($t/T_r = 0.01$ and 0.51) and two troughs ($t/T_r = 0.28$ and 0.78) of the infragravity wave become visible.

Ensemble-averaged, co-located measurements of u_∞ show good agreement between ACVP and ADV (Figure 6b) and u_∞ is in phase with the η-measurements shown previously (Figure 6a). There are large time-dependent gradients (accelerations) of u_∞ at phases of upcrossings and magnitudes of u_∞ are higher at velocity crest phases compared to velocity trough phases. In general, the short waves are visibly skewed and asymmetric, with the larger waves in the groups being more asymmetric (as reported for different experiments with bichromatic wave groups by *Padilla and Alsina* [2017]).

When observing the whole ACVP measuring domain from bed to emitter (Figure 6c), strong near-bed gradients in contrast to approximately depth-uniform velocities at higher elevations become visible. At phases of $u(z)$ crests, near-bed onshore velocities were higher than the free stream ones (e.g. compare $\zeta = 0.01$ to $\zeta = 0.045$ at $t/T_r = 0.16$).

In Figure 6a-c a variety of phase leads become visible. In water surface elevation measurements (Figure 6a), infragravity wave troughs would be expected to coincide with the largest short waves and infragravity wave crests with the smallest short waves. However, a phase shift between short waves and the associated infragravity wave becomes visible (e.g. *Battjes et al.* [2004] and *Padilla and Alsina* [2017]). When comparing the water surface elevations with free stream velocity measurements (Figure 6b), the short wave fluctuations of u_∞ and η are in phase but there is a phase shift between u_{ig} and η_{ig}. Additionally, phase leads between free stream and near-bed velocity are visible (e.g. Figure 6c at $t/T_r = 0.28$), with flow reversal close to the bed occurring earlier than at free-stream elevations. Such phase leads are typical for oscillatory boundary layers (e.g. *Sleath* [1987], *Jensen et al.* [1989] or *van der A et al.* [2011]).

The measurements of near–bed sediment concentration (Figure 6d) show double peaks (at $\zeta < 0.005$m, visible in expansion of yellow contours) before and after the upcrossings of the largest short waves (e.g. $t/T_r = 0.1$ and 0.155). They coincide with peaks in offshore and onshore velocity although often the double peaks look as one merged single peak especially up in the water column in comparison to elevations close to the bed. The concentration peaks during the velocity crests are larger than the ones during the troughs.

Moreover, high concentrations during the crests extend further up into the water column, resulting in expansion of the sheet flow layer. The higher peaks during the crests may be linked to the rapid accelerations under velocity upcrossings and the positive vertical velocity w at those phases. The sediment does not settle down fully during the time span between the velocity troughs and the following crests, indicating "phase lag effects" due to large sediment diffusivity (as defined in *Ribberink et al.* [2008]). This potentially indicates the influence of sediment advection from adjacent cross-shore locations and that sediment mobilized during the offshore wave phase is subsequently mobilized during the onshore phase. This partly results from the short duration between largest offshore and onshore velocity magnitudes in asymmetric waves and the relatively low settling velocity associated to a relatively fine sediment size. The sheet flow layer (delimited by the 8% volumetric concentration criterion [*Dohmen-Janssen et al.*, 2001]) is observed to expand at phases of largest short wave crests, in line with calculations from semi-empirical models (e.g. *Nielsen and Callaghan* [2003]).

At higher elevations ($\zeta > 0.01$m), plumes of suspended sediment are observed during upcrossings of the largest short waves. Their concentrations build up slowly before the upcrossings and, after their maxima, which are in phase with the upcrossings, decrease more rapidly. Furthermore, during the largest short waves the sediment does not settle down fully and it is mobilized importantly by the following wave even though the wave's velocity is not very large, e.g. waves 6 and 7 at $t/Tr = 0.8$. The origin of the sediment suspension plumes will be investigated in depth in section 5.5.

4.3.2. Outer surfzone

Similar figures to Figure 6 are now presented in shallower water depth and very close to the bar crest (0.1m offshore of it). This position is slightly onshore from the visually observed position of outer wave breaking (defined as the breaking location of the highest waves in the groups). The ensemble-averaged water surface elevations of the largest short waves (Figure 7a) show smaller crests and shallower troughs compared to positions further offshore, indicating breaking or initiation of breaking of the largest waves in the groups. In wave groups, wave breaking typically starts at the largest short waves in the group expanding to the adjacent waves and reducing the wave groups' modulation [*Padilla and Alsina*, 2017]. The previously-observed phase shift between short waves and associated infragravity wave is still visible, but less substantial than further offshore.

In comparison with the results further offshore, Figure 7b shows slightly worse agreement between ACVP and ADV, potentially because of higher breaking intensity. Due to reduced water depths, velocity magnitudes are higher and the signal is more saw tooth-shaped with higher horizontal velocity gradients at upcrossings than in Figure 6b.

Indications of a transition from large vertical gradient in velocity close to the bed to depth-constant velocity towards the upper end of the measuring domain are visible (Figure 7c, note the changing vector lengths). Again, phase leads between free stream and near-bed velocity and shorter onshore than offshore phases become visible.

Additionally, higher concentrations are observed throughout the whole repetition period (Figure 7d). Concentration plumes contain larger concentrations and have longer duration. In fact, suspended concentration does not have enough time to settle down throughout most of T_r and the distinction between the sediment peaks during the negative and positive velocity phases is even less clear than in Figure 6d. This indicates a larger impact of sediment advection and sediment diffusivity. These may be of special importance between the wave groups ($t/T_r = 0.3$ to 0.45 and 0.85 to 0.95), where suspended concentrations remain large at high vertical elevations (suspension) during consecutive waves (see also *Villard et al.* [2000], *O'Hara et al.* [2012] and *van der Zanden et al.* [2019b]). The increased suspension might be partly induced by larger velocity magnitudes and, most likely, by larger turbulent kinetic energy (*van der Zanden et al.* [2019a] and *Larsen et al.* [2020]).

In contrast to the other position, the intrawave bed elevation changes are more significant. A larger thickness of the sheet flow layer at phases of expansion, partly because of their coincidence with bed erosion, becomes visible. Additionally, more short waves now generate sheet flow expansions. This likely relates to the overall higher maximum instantaneous velocities and resulting bed shear, compared to the position further offshore. Furthermore, increasing velocity accelerations and the resulting increase in near-bed pressure gradients (e.g. *Anderson et al.* [2017] or [*Ruessink et al.*, 2011]) might play an important role as well.

4.4. Intrawave sediment transport

4.4.1. Shoaling region

Horizontal sediment flux over the repetition period (Figure 8) was obtained as the product of ensemble-averaged, co-located horizontal velocity and sediment concentration (shown in Figure 6c/d). The measured quantities were decomposed and integrated over depth as previously described (section 3.6). Figure 8 presents the measured fluxes in the shoaling region and includes the depth-integrated transport rates from the summation of ACVP and OBS/ADV data as dotted lines.

Total fluxes and transport rates (Figure 8a) fluctuate in phase with u_{sw} (not shown for brevity but evident from u_∞) and the largest fluxes and transport rates are associated with the largest short waves. Offshore transport occurs over longer durations than onshore transport. This may be related to the longer troughs and steeper crests of skewed waves but also to the time-averaged offshore current (Figure 5). Onshore flux at crest phases features higher magnitudes and notable flux magnitudes extend further up into the water column than during offshore fluxes.

The concentration signal, which is positive at all time instants, is decomposed based on the frequencies present while ensuring that the sum of decomposed components equals the input signal. At certain phases this requires that c_{sw} takes negative values. However, this does not mean "physically" negative, because the only physical measurement was taken of non-decomposed concentrations. Rather, the negative c_{sw} values should be interpreted in relation to the total, directly-measured concentration. Multiplication of such "negative" concentrations with velocities, however, may lead to confusion over the definition of onshore and offshore transports. Therefore, it was chosen to refer to decomposed sediment transports as either "positive" or "negative" instead of onshore or offshore and to interpret them with respect to a mean, decomposed value.

In the short wave component (Figure 8b), positive fluxes and transport rates are dominant, consistent with the asymmetry of the waves. Whereas positive flux extends further up into the water column, negative flux is confined to regions very close to the bed. Surprisingly, two crests and troughs can be observed over the phase of a single short wave (e.g. short wave 2). This results from the decomposition of velocity and concentration, as mentioned in the previous paragraph.

In the infragravity component (Figure 8c), negative transport is higher than positive transport and its duration is longer. Highest flux magnitudes are observed in the near-bed region ($\zeta < 0.01$m) and there are larger negative transport rates during the second wave group, which is consistent with its larger η_{ig} amplitude (Figure 6a). Surprisingly, four crests and troughs can be observed over T_r.

T_r contains two wave groups so that two crests and troughs of infragravity components should be expected. However, crests and troughs of infragravity velocity u_{ig} and concentration c_{ig} are phase shifted. In fact, calculations via cross-correlation indicate an approximately depth-uniform phase shift of roughly 90 degrees between u_{ig} and c_{ig}. Thus, two of the observed q_{ig} troughs (crests) result from multiplication of positive (negative) u_{ig} with negative c_{ig} and two from the multiplication of negative (positive) u_{ig} with positive c_{ig}. As explained in more detail in section 5.6, the phase shift between u_{ig} and c_{ig} originates from a phase shift between short wave envelope and infragravity wave, which affects sediment transport in two ways. On the one hand, infragravity waves transport the sediment stirred up by short waves and the phase shift affects their relative timing. On the other hand, short waves occurring at phases of infragravity wave troughs, rather than crests, are more effective in stirring sediment (smaller water depth).

Note that there is an additional decomposed transport component which is not shown as a separate panel in Figure 8. The current-related (mean) component of sediment transport results from time-averaging velocity and concentration separately before multiplying them. Therefore, it does not have an intrawave time series. Nevertheless, the total transport (Figure 8a) contains the influence of this component, which is mainly negative (offshore-directed; as shown in a detailed analysis in section 4.5). This leads to the offshore transports which are visible at certain phases in the total transport (e.g. Figure 8a $t/Tr = 0.25$) but not in the short wave-related transport (Figure 8b).

4.4.2. Outer surfzone

When observing sediment transports in a cross-shore position closer to the bar crest, the non-decomposed transport (Figure 9a) shows similar intrawave characteristics as mentioned previously for the shoaling zone. However, fluxes and transport rates are a factor 2-3 higher. The figure further shows that the crests and troughs of transport rate become more peaked, consistent with the more asymmetric wave shape. Furthermore, the vertical and temporal extents of onshore (offshore) flux during crest (trough) phases of the single short waves are larger.

In the decomposed fluxes (Figure 9b/c) data gaps at the upper end of the measuring domain become visible. As mentioned in section 3.5, decomposed quantities were calculated in the ζ'-coordinate system (Figure 2d) to ensure the continuity of time series in single bins. In the process, the phase with shortest vertical extent over T_r determines the vertical extent of measurements in the ζ'-coordinate system for all phases of T_r. This is because only bins with continuous information throughout T_r are accepted for decomposition. When shifting measurements back to the ζ-coordinate system for graphical representation, the data gaps become visible at phases of intrawave erosion. The position further offshore (Figure 8) did not feature the gaps in the shown vertical domain because the available vertical extent of measurements was much larger.

Similar to the total transport, the short wave fluxes and transport rates (Figure 9b) feature larger transport magnitudes (factor 2-3) as well as larger vertical and temporal extent of notable fluxes than further offshore. The double crests and troughs during single short waves have the same cause as described previously for the position further offshore.

The infragravity flux and transport rate (Figure 9c) show four troughs of near-bed negative transport, similar to the ones observed further offshore. They result from the same phase shift between u_{ig} and c_{ig} that was mentioned previously. Flux and transport rate magnitudes are much higher than further offshore (factor 5), but are of considerably lower magnitude than the short wave contributions (note the different scales). There are indications of opposing flux directions during the same phase at different elevations.

For brevity, only the intrawave plots of the most offshore and onshore test were presented. In the other tests substantial flux magnitudes were observed at higher elevations above the bed as well (even at $\zeta = 0.05$m and higher) and sheet flow thicknesses up to 1.5cm were measured. Nevertheless, their intrawave time series of fluxes and transport rates are conceptually very similar to the ones shown. Only in the infragravity component there was a notable difference. Whereas Figure 9c only slightly indicates a vertical separation of transport directions, this becomes much more evident in tests 53 and 54 and will be explained in detail in section 5.6.

4.5. Net sediment transport

4.5.1. Linking net transport rates and morphological evolution

Figure 10 serves to connect the previously observed morphological evolution to net sediment transport rates. As explained in section 3.3, the net transport rate which occurred during a single test in each cross-shore location can be calculated by inputting beach profile transect measurements into the Exner equation. Ensemble-averaging over all considered tests provides the red solid line shown in Figure 10a. To quantify the influence of error accumulation in residuals and measurement inaccuracies, the calculations were repeated without correction for residuals and with a shift of profile transect measurements by their inaccuracy (up and down 1cm). This provides the error bounds (red dashed lines) shown in Figure 10a. By depth-integrating and time-averaging ACVP and OBS/ADV instantaneous sediment transport measurements, net transport rate in single cross-shore locations (star and square markers respectively) can be obtained. When comparing their summation (circle markers) to the net transport rate from profile transect measurements, good agreement well within error bounds is observed.

Net offshore transport rate becomes visible over most of the region surrounding the outer bar crest (Figure 10a). Only on the offshore edge of the shown domain there is net onshore transport rate ($x' < -2$m in Figure 10a). The net offshore transport rate increases on the offshore side of the crest and decreases on its onshore side. The maximum in net offshore transport rate obtained from the Exner equation is located slightly onshore of the bar crest. The ACVP and OBS/ADV net transport rates follow a similar cross-shore evolution starting from onshore transport rate in offshore positions to increasing offshore transport rate in positions closer to the bar crest. However, their maximum in total (sum of ACVP and OBS/ADV contributions) net offshore transport rate is observed further offshore than from the Exner equation. In the breaking region, sediment might be suspended up to elevations above wave trough level, forming a notable onshore-directed transport contribution [*van der Zanden et al.*, 2017a]. This contribution is disregarded in the present approach, which might explain why the total transport rate by the combined ACVP and OBS/ADV measurements (circles) tends towards more negative values than the total transport rate obtained from the profile transect measurements.

The present variations in net transport rate indicate a distinct pattern of morphological evolution over the outer bar. Increase of net offshore transport rate on the offshore side of the bar ($x' < 0.5$m) results in erosion; decrease of net offshore transport rate on the onshore side of the bar ($x' > 0.5$m) results in accretion. At the same time, there is larger net offshore transport rate on the onshore side of the bar ($x' = 2$m) than on its offshore side ($x' = -2$m). In combination this leads to offshore migration of the bar, maintaining its general shape.

Resolving the vertical dimension of ACVP and OBS/ADV measurements (Figure 10b) provides additional detail on the net transport rates. In the most offshore position (test 36) the only substantial flux is observed close to the bed ($\zeta' < 2$cm) and it is onshore directed. At locations closer to the bar crest, the vertical extent and magnitude of near-bed onshore flux increases. At the same time, an increase in net offshore flux at higher elevations is observed in locations closer to the bar crest. In the shoaling region ($x' < -0.5$m), the available vertical domain of ACVP and OBS/ADV measurements captures all substantial net flux, as net flux magnitudes decrease towards its upper end. On the bar crest, however, offshore flux remains at the upper end of the vertical measurement domain (which is also slightly shorter than in other tests because of the significant bed evolution in the considered tests (53 and 105)). In general, net flux profiles are characterized by large magnitudes of net onshore flux over small vertical extents close to the bed and smaller magnitudes of net offshore flux over larger vertical extents at higher elevation above the bed.

4.5.2. Depth-resolving, decomposed net fluxes

To explain how different time scale-related processes contributed to the observed net transport rates, sediment fluxes were Reynolds-decomposed (Figure 11). Essentially, Figure 11 results from time-averaging of the intrawave time series shown in Figures 8 and 9. Summation of the decomposed net flux profiles (Figure 11b-d) results in the total net flux profile (Figure 11a).

The short wave-related component (Figure 11b) is characterized by large net onshore flux over a small vertical extent in the near-bed region. Maximum magnitudes are observed offshore of the bar crest ($-1 < x' < -0.5$m). The current-related component (Figure 11c) is characterized by large net offshore flux near the bed and smaller net offshore flux at higher elevations. Again, maximum magnitudes are observed offshore of the bar crest ($-1 < x' < -0.5$m). The infragravity-related component (Figure 11d) features much lower magnitudes than the other two components. It is characterized by net offshore flux near the bed and, in some cross-shore positions, net onshore flux at higher elevations ($0.03 < \zeta' < 0.1$m). In most cross-shore positions the short wave-related onshore flux is counteracted by the current-related offshore flux. Whereas the short wave-related onshore flux dominates near the bed, the current-related offshore flux does at higher elevations. The infragravity-related flux features both onshore and offshore contributions but has lower magnitudes than the other two components. A detailed explanation of the underlying sediment transport processes follows in section 5.1.

4.5.3. Depth-integrated, decomposed net transports rates

Figure 12 illustrates the cross-shore evolution of depth-integrated net transport rates associated with different transport components. Initially, the total transport rate is onshore-directed but it becomes more offshore-directed in positions closer to the bar crest (star markers in Figure 12a). The maximum of total net offshore transport rate is observed around 0.4m offshore of the bar crest. Short wave- and current-related transport rates have opposing directions but follow a similar cross-shore evolution. It is characterized by increasing transport rate magnitudes up to the maxima at $-1 < x' < -0.5$m followed by decrease further shoreward. Infragravity-related net transport rate is initially offshore-directed but, in contrast to short wave- and current-related components, changes sign further onshore. Bedload and suspended load follow a similar cross-shore evolution as short wave- and current-related transport components (Figure 12b). Similarly, they do not change sign and their magnitudes increase initially, followed by a decrease.

During the morphological evolution towards equilibrium, certain components are more important than others. When comparing different frequency ranges, infragravity net transport rate has the smallest magnitude. Large short wave- and current-related net transport rates determine the total net transport rate but cancel each other out. Therefore, the resulting total net transport rate was, in certain cross-shore positions, of similar magnitude as the infragravity net transport rate. When comparing the modes of transport, in most locations larger suspended net transport rates are observed, resulting in net offshore transport rate. Short wave-related net transport rate and bedload follow similar evolutions but the former has larger net magnitudes. The same applies to current-related net transport rate and suspended load.

5. Discussion

5.1. Sediment transport processes

The near-bed onshore flux (Figure 11a) results from short wave-related processes, which depend on short wave orbital motion, asymmetry and skewness (Figure 11b). Time series of c_{sw} close to the bed (not shown for brevity) show gradual increases of concentration during the velocity trough phases, but rapid concentration spikes of higher magnitude were observed at velocity crest phases. The mentioned correlations occur, more or less, during all short waves and have consequences for net transport. Even though u_{sw} trough phases are longer than u_{sw} crest phases, crest magnitudes are higher than trough magnitudes and c_{sw} is higher during crest phases. Additionally, near-bed velocity is observed to be phase-shifted ahead of u_{∞} (flow reversals inside the wave bottom boundary layer lead the free-stream elevations, e.g. Figure 7) which is consistent with expectations under asymmetric waves (e.g. *Sleath* [1987], *Jensen et al.* [1989] or *van der A et al.* [2011]). This limits the duration over which high concentrations are correlated with negative velocities and further contributes to positive transport. So that, overall, positive net flux occurs near the bed.

At higher elevations, c_{sw} concentration peaks occur closer to the upcrossings and are more evenly distributed on both sides of them (e.g. Figure 6). Furthermore, the change from offshore to onshore velocity occurs more precisely at the upcrossing. Therefore, the amounts of positive and negative q_{sw} are more similar at higher elevations. In combination with the low sediment concentrations at high elevations this leads to very low net flux at high elevations.

The cross-shore evolution of q_{sw} is associated to the cross-shore evolution of the short waves within the groups and the resulting sediment dynamics. Through shoaling during onshore propagation the orbital amplitude, skewness and asymmetry of short waves is known to increase. Once the waves start breaking, their orbital amplitude, skewness and asymmetry usually decrease again. Furthermore, the single short waves of a group become more similar through breaking – the group is demodulating. In the present study, the short waves were predominantly governed by shoaling in between $x' = -2.4$m (test 36) and $x' = -0.6$m (test 54) and predominantly governed by breaking onshore of $x' = -0.4$m. Therefore, it is not surprising that near-bed onshore flux magnitude and the vertical extent of onshore flux increased from $x' = -2.4$m to $x' = -0.6$m and decreased again after (Figure 11b).

For the current-related component (Figure 11c), the vertical distributions of time-averaged sediment concentrations and velocities are important. The former depends on many different factors including velocity shear stress (e.g. *Nielsen* [1992]), turbulence injection into the water column (e.g. *Deigaard et al.* [1986]) and advection-diffusion of concentration over the vertical and horizontal (e.g. *van der Zanden et al.* [2017a]). The latter depends on radiation stress gradients [*Longuet-Higgins and Stewart*, 1964], which, in turn, depend on wave breaking and profile slope, time-averaged onshore transport (e.g. *Svendsen* [1984]) and turbulent Reynolds stresses (e.g. *Larsen et al.* [2020]). Certainly, both time-averaged sediment concentration and velocity heavily depend on water depth and cross-shore position relative to the bar crest. In general, the time-averaged velocity profiles decreased in the near-bed region. The time-averaged concentration profiles, on the other hand, increased significantly in the near-bed region. This results in the high near-bed current-related flux peaks visible in Figure 11c.

Offshore of the bar crest (Figure 6d), continuously large concentrations were only observed very close to the bed ($\zeta' < 0.005$m). Closer to the bar crest, suspended sediment concentrations increased, resulting in constantly high concentrations at higher elevations, too (e.g. Figure 7d). At the same time, there was a cross-shore evolution of time-averaged velocities (Figure 5). Far offshore of the bar crest the influence of wave breaking and undertow is low so that nonlinear streaming [*Longuet-Higgins*, 1953] and onshore transport dominates (Figure 11c, test 36). Closer to the bar crest the influence of undertow becomes stronger and all current-related sediment flux is offshore-directed. The largest current-related offshore flux magnitude is observed at $x' = -0.6$m (Figure 11c, test 54), consistent with the position of largest time-averaged offshore velocity magnitude (Figure 5b, test 54).

Net flux contributions from the infragravity component (Figure 11d) are much lower than the ones from the short wave- and current-related components. As discussed in detail previously, magnitude and direction of its net flux depend on the correlation of c_{ig} and u_{ig}. They, in turn, depend on correlation of the wave group envelope and the infragravity wave, as explained in detail in section 5.6. At $-1.5 < x' < -0.5$m the correlations were such that a significant net transport rate from the infragravity component was measured (Figure 12a).

To explain how different elevation-related processes contributed to the observed net transport rates, sediment fluxes were integrated over different vertical layers associated with transport as bedload and suspended load. Bedload sediment transport rate may reach very high magnitudes because it occurs just above the seabed, where sediment concentrations are highest. A common way to define it, is that it occurs under the influence of intergranular forces [*Bagnold*, 1956]. In the absence of methods to measure those forces directly, a volumetric concentration threshold of 8% [*Dohmen-Janssen et al.*, 2001] is usually taken to delimit the sheet flow layer and, thus, the bedload transport. All transport below the corresponding intrawave varying elevation is considered bedload.

Thus, the net transport rate from bedload depends heavily on the magnitude and phasing of sheet flow layer thickness.

The T_r-resolving contour plots shown previously (Figures 6c/d and 7c/d) indicate larger sheet flow layer thicknesses at phases of short wave crests. At those phases the horizontal velocity is directed onshore and large onshore sediment fluxes and transport rates are visible. As this process clearly operates at the time scale of the short waves, a large proportion of the net onshore flux by the short wave component visible in Figure 11b is probably associated with bedload. At most of the other phases of T_r, the sheet flow layer limit is located just above the bed. Time-averaged offshore currents were shown to operate throughout T_r. In the near-bed region, their magnitude decreases rapidly (Figure 5a). Nevertheless, the remaining time-averaged currents act on large sediment concentrations, especially below the upper sheet flow layer limit. Therefore, part of the near-bed peak in net offshore flux by the current component (Figure 11c) is probably associated with bedload. Yet, the onshore bedload transport at short wave crest phases occurs over a large vertical extent and at high concentrations and velocity magnitudes. Thus, bedload transport rate is onshore-directed in all observed cross-shore positions (Figure 12b).

Suspended transport occurs whenever sediment particles in suspension are transported by instantaneous or time-averaged currents. Note that the present study considers particles inside the sheet flow layer as not in suspension (because of the intergranular forces, as mentioned previously). In suspended sediment transport the concentration magnitudes and, in consequence, flux magnitudes are lower than in bedload. However, it potentially occurs over larger parts of the water column, influencing net transport rates substantially.

At short wave timescale, there was no substantial suspended net flux (Figure 11b), as explained at the top of this subsection. On a time-averaged scale, suspended concentrations become more significant. Here, the transport direction was mainly offshore, leading to large net offshore fluxes in suspension (Figure 11c). At infragravity time-scale, there was some transport in suspension (Figure 11d). Interestingly, suspended transport at infragravity time-scale can be onshore- or offshore-directed. Ultimately, the total suspended transport rate is offshore-directed (Figure 12b).

5.2. Comparison to transport processes in other studies

The present data agree well with other large-scale experiments (*van der Zanden et al.* [2017a] and *Mieras et al.* [2019]) when considering the mode of sediment transport, either bedload or suspended load. Total net transport rate resulted from a balance of net offshore transport in suspension, mainly from the current-related component, and net onshore transport occurred as bedload, mainly from the short wave-related component. When net bedload was larger than net suspended load, net onshore transport rate resulted. In the present study and in the experiments of *van der Zanden et al.* [2017a] this occurred only offshore of the outer breaker bar crest ($x' < -2$m). In the experiments of *Mieras et al.* [2019], which focused on one cross-shore position (breaker bar crest), it occurred under the waves with larger wave height. Under the previously-mentioned conditions (offshore positions and large wave heights at the bar crest with wave breaking onshore of the crest), time-averaged offshore currents were relatively low and wave asymmetry, resulting in considerable onshore transport under short wave crests, takes an important role in sediment transport processes.

In contrast to the other experiments (*van der Zanden et al.* [2017a] and *Mieras et al.* [2019]), there was an infragravity-wave related transport component in the present study. Its net transport rate was much lower than the short wave- and current-related rates, but they opposed each other. As a result, in certain cross-shore position the magnitude of the net infragravity-related transport was considerable when compared to the total net transport magnitude and shows potential for influencing the total net transport direction ($-1.5 < x' < -0.5$m Figure 12a). In field experiments on the seaward side of bars, *Ruessink et al.* [1998] identified a similar importance of infragravity wave-related transport relative to short wave- and current-related transports which opposed each other.

5.3. Limitations

In contrast to other sediment transport studies with ensemble-averaging (e.g. *Mieras et al.* [2019]), the present experiments featured fully-evolving beach profiles. Thus, there may be doubt about the quasi-steadiness of hydro-morphodynamic conditions, which is required for ensemble-averaging. To assess this, the time-averaged free stream velocities in all ensembles of single tests were compared (not shown for brevity). No organized trends over the course of the tests became visible and the standard deviations of each population of 46 ensembles varied between 0.011 and 0.035m/s. Considering other complicating influences on the measurements of each ensemble, like turbulence, this variability is assumed low enough for ensemble-averaging to be applicable.

The present experiments only featured one type of sand ($D_{50} = 0.25$mm). Repetition of the experiments with coarser sand is expected to show reduced offshore bar migration. This is because grains would react more quasi-instantaneously to hydrodynamic forcing with less sediment suspension and less net offshore suspended transport, reducing total net offshore transport rate. Repetition with finer sand, on the other hand, might show increased offshore bar migration because of a less quasi-instantaneous reaction of grains. However, there is the complicating factor that the net short wave-related transport rate has been argued to reduce in very fine sands because of time lags [*Dohmen-Janssen et al.*, 2002]. Indeed, calculation of their phase lag parameter with values from the present experiments (not shown for brevity; use of measured sheet flow thicknesses and T_p) indicates no phase lag effects. But for a finer sand, like the fine one ($D_{50} = 0.13$mm) in *Dohmen-Janssen et al.* [2002], phase lag effects and net transport rate reduction would be expected in the short-wave related transport component (assuming the same or larger sheet flow layer thickness).

Furthermore, the present study is limited by the lack of detailed measurements on the shoreward side of the bar due to air bubble intrusion from breaking waves (section 3.4). To avoid such problems in the future, it is recommended to ensure that air bubbles do not penetrate into the measuring domain of acoustic instruments (e.g. through larger water depth or less violent breaking).

5.4. Transport processes onshore of the bar

In the absence of detailed ACVP measurements onshore of the bar, judgments on the local sediment transport processes will be based on less-detailed measurements and results from literature. Overall, it seems likely that net transport rates were still controlled by the balance of offshore-directed suspended transport and onshore-directed bedload transport (e.g. *van der Zanden et al.* [2017b]), which, on the seaward side of the bar, were linked to current- and short wave-related transport.

In regards to current-related, suspended net offshore transport, undertow magnitude was measured (in the excluded E2 tests) to stay constant on the bar's shoreward side ($0 < x' < 1$m) and to decrease further onshore ($x' > 1$m). This is consistent with expectations from experiments and numerical modeling (e.g. *Garcez-Faria et al.* [2000] or *Boers* [2005], Fig. 2.17). The other factor determining current-related net transport, time-averaged concentration, was not measured at sufficient detail.

Related measurement problems originated from air bubbles which indicate increased levels of turbulence in the water column. As turbulence and sediment suspension are inherently linked, see *Aagaard et al.* [2021] for example, this indicates that sediment suspension at $0 < x' < 1.5$m was either similar or larger than further onshore ($-0.5 < x' < 0$m) – which is supported by various studies that linked turbulence from wave breaking to increased sediment suspension (e.g. *Yu et al.* [1993] or *Zhou et al.* [2017]). Thus, one might expect current-related, suspended net offshore transport to stay constant or increase on the bar's onshore side ($0 < x' < 1.5$m).

In regards to short wave-related, bedload net onshore transport, hydrodynamics on the shoreward side of the bar ($0 < x' < 1.5$m; in the excluded E2 tests), show reduced short wave velocity amplitudes and very asymmetric short wave velocity time series. Bedload is generally accepted (and often modeled) to depend on free stream velocity to a certain power (e.g. *Ribberink* [1998]), so that a decreased velocity amplitude should decrease net onshore transport rate. Short wave asymmetry has been linked to net onshore transport rate in various experiments (e.g. *Ruessink et al.* [2009] or *Kim et al.* [2019]) and increased asymmetry would be expected to increase net onshore transport rate [*van der A et al.*, 2010]. Thus, the changes in short wave-related, bedload net onshore transport would depend on the balance of these two competing processes.

Calculations with the Exner equation indicate a decrease in net offshore transport rates (Figure 10a, $0.4 < x' < 1.5$m). This is consistent with the balance between the previously-mentioned processes shifting more towards asymmetry-related net onshore transports rather than undertow-related net offshore transports. Note that there may be additional complicating factors like transport due to steep local bed slopes (e.g. *van der Zanden et al.* [2017b]), a process often considered in numerical modeling as well (e.g. *Bailard* [1981] or *Fernández-Mora et al.* [2015]).

5.5. Suspended sediment concentration plumes

In the sheet flow layer the present experiments show a rapid response of sediment concentration to flow velocity, without evidence of significant phase lags. Above the sheet flow layer, however, plumes of suspended sediment concentration not directly correlated with velocity were observed. *van der Zanden et al.* [2017a] observed similar suspended sediment plumes as shown in Figures 6d and 7d. They linked them to the horizontal (by advection) instead of vertical exchange of sediment. As visible in Figure 5, the time-averaged current is offshore-directed in the present experiments. Therefore, suspended sediments were, in general, advected offshore. Furthermore, the time-averaged offshore current under wave groups fluctuates in magnitude, which makes horizontal transports from cross-shore gradients in velocity more likely.

5.6. Details of infragravity sediment transport

The cross-shore evolution of H_{ig} in Figure 3 indicates a quasi-standing wave pattern, which is reaffirmed by the surfbeat similarity parameter, $\xi_{surfbeat}$ [*Baldock*, 2012], amounting to 0.306. A similar pattern was observed in the same wave flume by *Alsina et al.* [2016] and a similar result to their Figure 13a was obtained during data analysis in the present study (Figure 13). At cross-shore positions around the outer breaker bar, phase shifts between η_{ig} and η_{sw} of 45 to 90 degrees were measured. On dissipative beaches ($\xi_{surfbeat} < 0.02$) up to the start of short wave breaking, infragravity waves are dominated by second order energy transfers from short waves. As a result, they are 180 degrees out of phase with the short wave envelope (e.g. *Battjes et al.* [2004]). On intermediate or steep beach slopes, however, breakpoint infragravity wave generation (e.g. *Symonds et al.* [1982] or *Baldock et al.* [2000]) and reflection of the ingoing infragravity wave (e.g. *Padilla and Alsina* [2018]) become important as well and influence the phase shift. Therefore, the influence of phase shifts between η_{ig} and η_{sw} changes with cross-shore location because of the distance to breakpoint and shoreline [*Padilla and Alsina*, 2018]. The phase shift between η_{ig} and η_{sw} causes, in turn, a phase shift between u_{ig} and c_{ig} as mentioned earlier (section 4.4.1). This resulted in four crests and troughs of infragravity sediment fluxes and transport rates (Figures 8c and 9c).

Opposing flux directions over the vertical became visible in the infragravity component in positions close to the bar crest (Figure 9c and Figure 11d, tests 53, 54 and 105). These are related to differences in sediment suspension. Near the bed, c_{ig} (not shown for brevity) is heavily influenced by sediment suspension at short wave time scale and maxima occur at times of largest short waves. This applies in all the observed relative cross-shore positions. Higher in the water column ($\zeta' > 0.015$m), there is no considerable c_{ig} in offshore positions (e.g. tests 36 or 39). Closer to the bar crest (tests 53, 54 and 105), however, there is more suspension to higher elevations and sediment stays in suspension during the smaller short waves that mark the transition from one wave group to the next (e.g. Figure 7d, $t/T_r = 0.3 - 0.4$). As a result, the maxima of c_{ig} are found at times of the smallest short waves. This leads to the opposing infragravity net flux direction at higher elevation.

Different studies have reported both onshore and offshore net transport rates from the infragravity component (e.g. *Osborne and Greenwood* [1992], *Alsina and Cáceres* [2011], *Cáceres et al.* [2016] and *de Bakker et al.* [2016]). The presence of free and bound infragravity waves and the correlation of the infragravity velocity with the wave group structure, which in turn dominates the infragravity sediment concentration, is the main factor explaining the infragravity sediment transport direction – see for example *de Bakker et al.* [2016] for a resumed conceptual model. When considering the present results, the question arises whether infragravity sediment fluxes measured with OBSs have been obtained in the net onshore or the net offshore part of the infragravity net flux profile as it is very difficult to track the bed elevation during field experiments. The present measurements show the importance of measuring infragravity sediment flux profiles instead of single elevations to obtain a reliable depth-integrated result (sediment transport rate). Nevertheless, the presented results agree well with previous works obtained in similar conditions, i.e. a moderate beach slope and relatively small infragravity frequency showing a dependence between infragravity sediment flux and cross-shore infragravity wave pattern (e.g. *Alsina and Cáceres* [2011]; *Cáceres et al.* [2016] and *de Bakker et al.* [2016]). A quasi-standing wave pattern was observed to influence the phase shift between u_{ig} and

c_{ig}, which determines the direction of net flux. Furthermore, phase shifts might change after wave breaking as the group loses modulation (see *Padilla and Alsina* [2017]).

6. Conclusion

Sediment transport processes near the seabed were investigated through a large-scale wave flume experiment with erosive ($\Omega = 2.54$), bichromatic wave groups over a morphologically-evolving beach of medium sand. Apart from standard instrumentation in various cross-shore positions, tests featured detailed near-bed measurements of co-located velocity, sediment concentration and sediment flux profiles in single cross-shore positions. Normalization of cross-shore and vertical positions relative to the outer breaker bar position and elevation allowed the analysis of near-bed hydrodynamics and sediment transport processes during erosive beach profile evolution (offshore bar migration) in a quasi-steady equilibrium state. Aggregation over 6 tests ranging from shoaling to breaking zone provided insights into the processes' cross-shore evolution. To investigate processes further, measurements were frequency-filtered and divided into transport modes (bedload and suspended load). Based on the results we conclude the following:

1. Total net transport rate mainly resulted from a balance of onshore-directed short wave-related transport near the bed and offshore-directed current-related transport. The short wave-related transport occurred mainly as bedload whereas the current-related transport occurred both as bedload and suspended load.

2. Infragravity wave-related fluxes were of much lower magnitude than short wave- and current-related fluxes. However, when short wave- and current-related net fluxes canceled out in certain cross-shore positions, the infragravity wave-related net fluxes formed a distinct contribution to the total net transport rate. Interestingly, some infragravity net flux

profiles featured opposing directions between near-bed offshore-directed and suspended onshore-directed sediment flux.

3. The outer bar offshore migration resulted from a cross-shore gradient in net offshore transport rate on the bar's offshore slope. This increase in net offshore transport rate, in turn, resulted from a stronger increase in current-related (mostly suspended) offshore transport than short wave-related (mostly bedload) onshore transport on the bar slope. The stronger increase in current-related transport only partly results from net flux magnitudes because the vertical extent of fluxes is a very important factor as well. Onshore flux was confined to the near-bed region whereas offshore flux occurred over large parts of the water column.

4. Closer to the outer bar crest, (instantaneous and time-averaged) suspended sediment concentrations were higher and sheet flow layer thicknesses were larger, compared to locations further offshore. Sediment suspension plumes above sheet flow layer elevations indicated that not only vertical but also horizontal exchange of sediment was important.

5. The main sediment suspension events were linked to short wave crests. Yet, net suspended transport by short waves was very low because fluxes under crests and troughs balanced each other. The net suspended transport by currents was considerable, because time-averaged currents were always directed offshore. The net suspended transport by infragravity waves was affected by concentration processes not only related quasi-instantaneously to short wave crests but also to the complicated phase relationship with infragravity wave velocities.

The present experimental data feature a combination of realistic representation of natural conditions (e.g. large-scale experiments, bichromatic waves and fully-evolving beach profiles) with the high detail of measurements (e.g. multiple cross-shore locations, very high vertical resolution in lowest 20cm and continuous bed tracking for referencing of measurements) only possible in the laboratory. Therefore, they represent a further step in providing detailed hydrodynamic and sediment transport information needed for a better understanding of bar morphodynamics and related sediment transport processes. As such, they may contribute to the further development of (process-based) numerical models. The complete set of data presented in this article can be consulted online (see Acknowledgements). Future work will focus on detailed measurements under the accretive wave conditions in RESIST.

Acknowledgments.

The experiments described in this work were funded by the European Communitys Horizon 2020 Programme through the grant to the budget of the Integrated Infrastructure Initiative HYDRALAB+, Contract no. 654110, and were conducted as part of the transnational access project RESIST. FG acknowledges funding from the Agency for Management of University and Research Grants (AGAUR). DH acknowledges funding from the French DGA funded ANR ASTRID Maturation project MESURE (ANR-16- ASMA-0005-01). JA acknowledges funding from the Serra Hnter Programme (SHP). We wish to thank fellow RESIST researchers and the CIEM staff (Joaquim Sospedra, Oscar Galego, Dr. Andrea Marzeddu) for their contributions to the experiments. For data related to this article visit: https://doi.org/10.5281/zenodo.5727127.

References

Aagaard, T., Brinkkemper, J., Christensen, D. F. Hughes, M. G., Ruessink, G. (2021). Surf Zone Turbulence and Suspended Sediment Dynamics–A Review. *Journal of Marine Science and Engineering*, *9*, *11*, *1300*. doi:10.3390/jmse9111300.

Alsina, J. M. and Cáceres, I. (2011). Sediment suspension events in the inner surf and swash zone. *Coastal Engineering*, *58* , *8*, 657–670. doi:10.1016/j.coastaleng.2011.03.002.

Alsina, J. M., Cáceres, I., Brocchini, M. and Baldock, T. E. (2012). An experimental study on sediment transport and bed evolution under different swash zone morphological conditions. *Coastal Engineering*, *68*, 31–43. doi:10.1016/j.coastaleng.2012.04.008.

Alsina, J. M., Padilla, E. M. and Cáceres, I. (2016). Sediment transport and beach profile evolution induced by bi-chromatic wave groups with different group periods. *Coastal Engineering*, *114*, 325–340. doi:10.1016/j.coastaleng.2016.04.020.

Anderson, D., Cox, D., Mieras, R., Puleo, J. A., and Hsu, T.-J. (2017). Observations of wave-induced pore pressure gradients and bed level response on a surf zone sandbar. *Journal of Geophysical Research: Oceans*, *122*, *6*, 5169–5193. doi: 10.1002/2016JC012557.

Bagnold, R. A. (1956). The flow of cohesionless grains in fluids. *Philos. Trans. R. Soc. A: Math. Phys. Eng. Sci.*, *249*, *964*, 235–297. doi:10.1098/rsta.1956.0020.

Bailard, J. A. (1981). An energetics total load sediment transport model for a plane sloping beach. *Journal of Geophysical Research: Oceans*, *86*, *C11*, 10938–10954. doi: 10.1029/JC086iC11p10938.

Baldock, T. E.,Huntley, D. A., Bird, P. A. D., O'Hare, T., Bullock, G. N. (2000). Breakpoint generated surf beat induced by bichromatic wave groups. *Coastal Engineering*, *39*, *2–4*, 213–242. doi:10.1016/S0378-3839(99)00061-7.

Baldock, T. E., Alsina, J. M., Cáceres, I., Vicinanza, D., Contestabile, P., Power, H. and Sánchez-Arcilla, A. (2011). Large-scale experiments on beach profile evolution and surf and swash zone sediment transport induced by long waves, wave groups and random waves. *Coastal Engineering*, *58*, *2*, 214–227. doi:10.1016/j.coastaleng.2010.10.006.

Baldock, T. E. (2012). Dissipation of incident forced long waves in the surf zoneImplications for the concept of bound wave release at short wave breaking. *Coastal Engineering*, *60*, 276–285. doi:10.1016/j.coastaleng.2011.11.002.

Battjes, J. A., Bakkenes, H. J., Janssen, T. T. and van Dongeren, A. R. (2004). Shoaling of subharmonic gravity waves. *Journal of Geophysical Research: Oceans*, *109*, *C02009.* doi:10.1029/2003JC001863.

Boers, M. (2005). Surf Zone Turbulence. *Doctoral thesis, TU Delft, The Netherlands.* Available at: http://resolver.tudelft.nl/uuid:71428ad5-0658-49f7-b83e-0deb26b668cf.

Bosman, J. J., van der Velden, E. T. J. M., and Hulsbergen, C. H. (1987). Sediment concentration measurement by transverse suction. *Coastal Engineering*, *11*, *4*, 353–370. doi:10.1016/0378-3839(87)90033-0.

Brinkkemper, J. A., Aagaard, T., de Bakker, A. T. M. and Ruessink, B. G. (2018). Shortwave Sand Transport in the Shallow Surf Zone. *Journal of Geophysical Research: Oceans*, *123*, *5*,1145–1159. doi:10.1029/2017JF004425.

Cáceres, I. and Alsina, J. M. (2016). Suspended sediment transport and beach dynamics induced by monochromatic conditions, long waves and wave groups. *Coastal Engineering*, *108*, 36–55. doi:10.1016/j.coastaleng.2015.11.004.

Cáceres, I., Alsina, J. M., van der Zanden, J., van der A., D. A., Ribberink, J. S. and Sánchez-Arcilla, A. (2020). The effect of air bubbles on optical backscatter sensor measurements under plunging breaking waves. *Coastal Engineering*, *159*, 103721. doi:10.1016/j.coastaleng.2020.103721.

Chassagneux, F. X. and Hurther, D. (2014). Wave bottom boundary layer processes below irregular surfzone breaking waves with light-weight sheet flow particle transport. *Journal of Geophysical Research: Oceans*, *119*, *3*,1668–1690. doi:10.1002/2013JC009338.

de Bakker, A. T. M., J. A. Brinkkemper, F. van der Steen, M. F. S. Tissier, and B. G. Ruessink (2016). Cross-shore sand transport by infragravity waves as a function of beach steepness. *Journal of Geophysical Research: Oceans*, *121*, *10*, 1786–1799. doi: 10.1002/2016JF003878.

Deigaard, R., Fredsøe, J. and Hedegaard, I. B. (1986). Suspended sediment in the surf zone. *Journal of Waterway, Port, Coastal and Ocean Engineering*, *112*, *1*, 115–128. doi:10.1061/(ASCE)0733-950X(1986)112:1(115).

Dohmen-Janssen, C. M., Hassan, W. N. and Ribberink, J. S. (2001). Mobile-bed effects in oscillatory sheet flow. *Journal of Geophysical Research: Oceans*, *106*, *C11*, 27103-27115. doi:10.1029/2000JC000513.

Dohmen-Janssen, C. M., Kroekenstoel, D. F., Hassan, W. N. and Ribberink, J. S. (2002). Phase lags in in oscillatory sheet flow: experiments and bed load modelling. *Coastal Engineering*, *46*, *1*, 61-87. doi:10.1016/S0378-3839(02)00056-X.

Downing, J. P. and Beach, R. A. (1989). Laboratory apparatus for calibrating optical suspended solids sensors. *Marine Geology*, *86*, *2–3*, 243-249. doi:10.1016/0025-3227(89)90053-4.

Dubarbier, B., Castelle, B., Marieu, V. and Ruessink, B. G. (2015). Process-based modeling of cross-shore sandbar behavior. *Coastal Engineering*, *95*, 35–50. doi:10.1016/j.coastaleng.2014.09.004.

Eichentopf, S., Cáceres, I. and Alsina, J. M. (2018). Breaker bar morphodynamics under erosive and accretive wave conditions in large-scale experiments. *Coastal Engineering*, *138*, 36–48. doi:10.1016/j.coastaleng.2018.04.010.

Eichentopf, S., van der Zanden, J., Cáceres, I. and Alsina, J. M. (2019). Beach Profile Evolution towards Equilibrium from Varying Initial Morphologies. *Journal of Marine Science and Engineering*, *7*, *11*, 406. doi:10.3390/jmse7110406.

Eichentopf, S., van der Zanden, J., Cáceres, I., Baldock, T. E. and Alsina, J. M. (2020). Influence of storm sequencing on breaker bar and shoreline evolution in large-scale experiments. *Coastal Engineering*, *157*, 103659. doi:10.1016/j.coastaleng.2020.103659.

Fernández-Mora, A., Calvete, D., Falqués, A., and de Swart, H. E. (2015). Onshore sandbar migration in the surf zone: New insights into the wave-induced sediment transport mechanisms. *Geophys. Res. Lett.*, *42*, *8*, 2869–2877. doi:10.1002/2014GL063004.

Fromant, G., Mieras, R. S., Revil-Baudard, T., Puleo, J. A., Hurther, D. and Chauchat, J. (2018). On Bedload and Suspended Load Measurement Performances in Sheet Flows Using Acoustic and Conductivity Profilers. *Journal of Geophysical Research: Earth Surface*, *123*, *10*, 2546–2562. doi:10.1029/2017JF004560.

Fromant, G., Hurther, D., van der Zanden, J., van der A., D. A., Cáceres, I., O'Donoghue, T. and Ribberink, J. S. (2019). Wave Boundary Layer Hydrodynamics and Sheet Flow Properties Under Large-Scale Plunging-Type Breaking Waves. *Journal of Geophysical Research: Oceans*, *124*, *1*, 75–98. doi:10.1029/2018JC014406.

Gallagher, E. L., Elgar, S., and Guza, R. T. (1998). Observations of sand bar evolution on a natural beach. *Journal of Geophysical Research: Oceans*, *103*, *C2*, 3203–3215. doi:10.1029/97JC02765.

Faria, A. F. G., Thornton, E. B., Lippmann, T. C., and Stanton, T. P. (2000). Undertow over a barred beach. *Journal of Geophysical Research: Oceans*, *105*, *C7*, 16999–17010. doi:10.1029/2000JC900084.

Goring, D. G. and Nikora, V. I. (2002). Despiking Acoustic Doppler Velocimeter Data. *Journal of Hydraulic Engineering*, *128 1*, 117–126. doi:10.1061/(ASCE)0733-9429(2002)128:1(117).

Henderson, S. and Allen, J. (2004). Nearshore sandbar migration predicted by an eddy-diffusive boundary layer model. *Journal of Geophysical Research: Oceans*, *109*, *C06024*. doi:10.1029/2003JC002137.

Hoefel, F. and Elgar, S. (2003). Wave-Induced Sediment Transport and Sandbar Migration. *Science*, *299*, *5614*, 1885–1887. doi:10.1126/science.1081448.

Hsu, T-J., Elgar, S. and Guza, R. T. (2006). Wave-induced sediment transport and onshore sandbar migration. *Coastal Engineering*, *53*, *10*, 817–824. doi:10.1016/j.coastaleng.2006.04.003.

Hurther, D. and Thorne, P. D. (2011). Suspension and nearbed load sediment transport processes above a migrating, sand-rippled bed under shoaling waves. *Journal of Geophysical Research: Oceans*, *116*, *C07001*. doi:10.1029/2010JC006774.

Hurther, D., Thorne, P. D., Bricault, M., Lemmin, U. and Barnoud, J.-M. (2011). A multi-frequency Acoustic Concentration and Velocity Profiler (ACVP) for boundary layer measurements of fine-scale flow and sediment transport processes. *Coastal Engineering*, *58*, *7*, 594–605. doi:10.1016/j.coastaleng.2011.01.006.

Jensen, B., Sumer B. and Fredsøe, J. (1989). Turbulent oscillatory boundary layers at high Reynolds numbers. *Journal of Fluid Mechanics*, *206*, 265–297. doi:10.1017/S0022112089002302.

Kim, Y., Mieras, R. S., Cheng, Z., Anderson, D., Hsu, T.-J., Puleo, J. A. and Cox, D. (2019). A numerical study of sheet flow driven by velocity and acceleration skewed near-breaking waves on a sandbar using SedWaveFoam. *Coastal Engineering*, *152*, 103526. doi:10.1016/j.coastaleng.2019.103526.

Larsen, B. E., van der A, D. A., van der Zanden, J., Ruessink, B. G. and Fuhrman, D. R. (2020). Stabilized RANS simulation of surf zone kinematics and boundary layer processes beneath large-scale plunging waves over a breaker bar. *Ocean Modelling*, *155*, 101705. doi:10.1016/j.ocemod.2020.101705.

Lanckriet, T., Puleo, J. A., and Waite, N. (2013). A conductivity concentration profiler for sheet flow sediment transport. *IEEE Journal of Oceanic Engineering*, *38*, *1*, 55–70. doi:10.1109/JOE.2012.2222791.

Longuet-Higgins, M. S. (1953). Mass transport in water waves. *Philosophical Transactions of the Royal Society of London. Series A, Mathematical and Physical Sciences*, *245*, *903*, 535–581. doi:10.1098/rsta.1953.0006.

Longuet-Higgins, M. S. and Stewart, R. W. (1964). Radiation stresses in water waves; a physical discussion, with applications. *Deep Sea Research and Oceanographic Abstracts*, *11*, *4*, 529–562. doi:10.1016/0011-7471(64)90001-4.

Mariño-Tapia, I. J., Russel, P. E., O'Hare, T. J., Davidson, M. A. and Huntley, D. A. (2007a). Cross-shore sediment transport on natural beaches and its relation to sandbar migration patterns: 1. Field observations and derivation of a transport parameterization. *Journal of Geophysical Research: Oceans*, *112*, *C03001*. doi: 10.1029/2005JC002893.

Mariño-Tapia, I. J., O'Hare, T. J., Russel, P. E., Davidson, M. A. and Huntley, D. A. (2007b). Crossshore sediment transport on natural beaches and its relation to sandbar migration patterns: 2. Application of the field transport parameterization. *Journal of Geophysical Research: Oceans*, *112*, *C03002*. doi:10.1029/2005JC002894.

Mieras, R. S., Puleo, J. A., Anderson, D., Hsu, T.J., Cox, D. T., and Calantoni, J. (2019). Relative contributions of bed load and suspended load to sediment transport under skewed-asymmetric waves on a sandbar crest. *Journal of Geophysical Research: Oceans*, *124*, *2*, 1294–1321. doi:10.1029/2018JC014564.

Moura, T. and Baldock, T. E. (2017). Remote sensing of the correlation between breakpoint oscillations and infragravity waves in the surf and swash zone. *Journal of Geophysical Research: Oceans*, *122*, *4*, 3106–3122. doi:10.1002/2016JC012233.

Nielsen, P. (1992). Coastal Bottom Boundary Layers and Sediment Transport. World Scientific, Singapore. doi:10.1142/1269.

Nielsen, P. and Callaghan, D. P. (2003). Shear stress and sediment transport calculations for sheet flow under waves. *Coastal Engineering*, *47*, *3*, 347–354. doi:10.1016/S0378-3839(02)00141-2.

O'Donoghue, T. and Wright, S. (2004a). Concentrations in oscillatory sheet flow for well sorted and graded sands. *Coastal Engineering*, *50*, *3*, 117–138. doi:10.1016/j.coastaleng.2003.09.004.

O'Donoghue, T. and Wright, S. (2004b). Flow tunnel measurements of velocities and sand flux in oscillatory sheet flow for well-sorted and graded sands. *Coastal Engineering*, *51*, *11–12*, 1163–1184. doi:10.1016/j.coastaleng.2004.08.001.

O'Hara Murray, R. B., Hodgson, D. M. and Thorne, P. D. (2012). Wave groups and sediment resuspension processes over evolving sandy bedforms. *Continental Shelf Research*, *46*, 16–30. doi:10.1016/j.csr.2012.02.011.

Osborne, P. D. and Greenwood, B. (1992). Frequency dependent cross-shore suspended sediment transport. 2. A barred shoreface. *Marine Geology*, *106*, *1–2*, 25–51. doi:10.1016/0025-3227(92)90053-K.

Padilla, E. M. and Alsina, J. M. (2017). Transfer and dissipation of energy during wave group propagation on a gentle beach slope. *Journal of Geophysical Research: Oceans*, *122*, *8*, 6773–6794. doi:10.1002/2017JC012703.

Padilla, E. M. and Alsina, J. M. (2018). Long Wave Generation Induced by Differences in the WaveGroup Structure. *Journal of Geophysical Research: Oceans*, *123*, *12*, 8921–8940. doi:10.1029/2018JC014213.

Pape, L., Plant, N. G. and Ruessink, B. G. (2010). On cross-shore migration and equilibrium states of nearshore sandbars. *Journal of Geophysical Research: Oceans*, *115*, *F03008*. doi:10.1029/2009JF001501.

Plant, N. G., Holman, R. A., Freilich, M. H. and Birkemeier, W. A. (1999). A simple model for interannual sandbar behavior. *Journal of Geophysical Research: Oceans*, *104*, *(C7)*, 15755–15776. doi:10.1029/1999JC900112.

Ribberink, J.S. and Al-Salem, A. (1992). Time-dependent sediment transport phenomena in oscillatory boundary-layer flow under sheet-flow conditions. *Delft Hydraulics, The*

Netherlands, Report H840.20 Part VI (Kustgenese/MaST).

Ribberink, J. S. (1998). Bed-load transport for steady flows and unsteady oscillatory flows. *Coastal Engineering*, *34*, *1–2*, 59–82. doi:10.1016/S0378-3839(98)00013-1.

Ribberink, J. S., van der Werf, J. J., O'Donoghue, T. and Hassan, W. N. M. (2008). Sand motion induced by oscillatory flows: Sheet flow and vortex ripples. *Journal of Turbulence*, *9*. doi:10.1080/14685240802220009.

Ruessink, B. G., Houwman, K. T. and Hoekstra, P. (1998). The systematic contribution of transporting mechanisms to the cross-shore sediment transport in water depths of 3 to 9 m. *Marine Geology*, *152*, *4*, 295–324. doi:10.1016/S0025-3227(98)00133-9.

Ruessink, B. G., van den Berg, T. J. J., and van Rijn, L. C. (2009). Modeling sediment transport beneath skewed asymmetric waves above a plane bed. *Journal of Geophysical Research: Oceans*, *114*, *C11021*. doi:10.1029/2009JC005416.

Ruessink, B. G., Michallet, H., Abreu, T., Sancho, F., Van der A, D. A., Van der Werf, J. J., and Silva, P. A. (2011). Observations of velocities, sand concentrations, and fluxes under velocity-asymmetric oscillatory flows. *Journal of Geophysical Research: Oceans*, *116*, *C03004*. doi:10.1029/2010JC006443.

Sleath, J. (1987). Turbulent oscillatory flow over rough beds. *Journal of Fluid Mechanics*, *182*, 369–409. doi:10.1017/S0022112087002374.

Svendsen, I. A. (1984). Mass flux and undertow in a surf zone. *Coastal Engineering*, *8*, *4*, 347–365. doi:10.1016/0378-3839(84)90030-9.

Symonds, G., Huntley, D. A. and Bowen, A. J. (1982). Two-dimensional surf beat: Long wave generation by a time-varying breakpoint. *Journal of Geophysical Research: Oceans*, *87*, *(C1)*,492–498. doi:10.1029/JC087iC01p00492.

van der A, D., O'Donoghue, T., and Ribberink, J. (2010). Measurements of sheet flow transport in acceleration-skewed oscillatory flow and comparison with practical formulations. *Coastal Engineering*, *57*, *3*, 331–342. doi:10.1016/j.coastaleng.2009.11.006.

van der A, D., O'Donoghue, T., Davies, A. and Ribberink, J. (2011). Experimental study of the turbulent boundary layer in acceleration-skewed oscillatory flow. *Journal of Fluid Mechanics*, *684*, 251–283. doi:10.1017/jfm.2011.300.

van der Zanden, J., van der A., D. A., Hurther, D., Cáceres, I., O'Donoghue, T. and Ribberink, J. S. (2017a). Suspended sediment transport around a large-scale laboratory breaker bar. *Coastal Engineering*, *125*, 51–69. doi:10.1016/j.coastaleng.2017.03.007.

van der Zanden, J., van der A., D. A., Hurther, D., Cáceres, I., O'Donoghue, T., Hulscher, S. J. M. H. and Ribberink, J. S. (2017b). Bedload and suspended load contributions to breaker bar morphodynamics. *Coastal Engineering*, *129*, 74–92. doi:10.1016/j.coastaleng.2017.09.005.

van der Zanden, J., van der A., D. A., Cáceres, I., Larsen, B. E., Fromant, G., Petrotta, C., Scandura, P. and Li, M. (2019a). Spatial and temporal distributions of turbulence under bichromatic breaking waves. *Coastal Engineering*, *146*, 65–80. doi:10.1016/j.coastaleng.2019.01.006.

van der Zanden, J., van der A., D. A., Thorne, P. D., O'Donoghue, T. and Ribberink, J. S. (2019b). Sand suspension and fluxes by wave groups and equivalent monochromatic waves. *Continental Shelf Research*, *179*, 85–104. doi:10.1016/j.csr.2019.04.005.

van Rijn, L. C., Tonnon, P. K. and Walstra, D. J. R. (2011). Numerical modelling of erosion and accretion of plane sloping beaches at different scales. *Coastal Engineering*, *58*, *7*, 637–655. doi:10.1016/j.coastaleng.2011.01.009.

Villard, P. V., Osborne, P. D. and Vincent, C. E. (2000). Influence of wave groups on SSC patterns over vortex ripples. *Continental Shelf Research*, *20*, *17*, 2391–2410. doi: 10.1016/S0278-4343(99)00068-0.

Wright, L. D. and Short, A. C. (1984). Morphodynamic variability of surf zones and beaches: A synthesis. *Marine Geology*, *56*, *1–4*, 93–118. doi:10.1016/0025-3227(84)90008-2.

Yu, Y., Sternberg, R. W. and Beach, R. A. (1993). Kinematics of breaking waves and associated suspended sediment in the nearshore zone. *Continental Shelf Research*, *13*, *11*, 1217–1242. doi:10.1016/0278-4343(93)90050-8.

Zedel, L., Hay, A. E., Wilson, G. W., and Hare, J. (2021). Pulse coherent doppler profiler measurement of bedload transport. *Journal of Geophysical Research: Oceans*, *126*, *e2020JF005572*. doi:10.1029/2020JF005572.

Zhou, Z., Hsu, T.-J., Cox, D., and Liu, X. (2017) (2017). Large-eddy simulation of wave-breaking induced turbulent coherent structures and suspended sediment transport on a barred beach. *Journal of Geophysical Research: Oceans*, *122*, *1*, 207–235. doi:10.1002/2016JC011884.

Table 1. Wave sequences in RESIST with measured wave conditions. Highlighted rows contain the tests for detailed analysis in this study.

Sequence	Test Number	Wave Condition	H_{rms}	T_p	T_g	Duration [min]	Ω [-]
	16	B	0.3	4	n/a	30	2.21
	17–23	E1	0.42	3.7	14.79	240	3.34
1	24–35	A1	0.23	4.7	33.68	600	1.44
	36–39	E2	0.32	3.7	14.79	120	2.54
	40–51	A1	0.23	4.7	33.68	600	1.44
	52	B	0.3	4	n/a	30	2.21
	53–56	E2	0.32	3.7	14.79	120	2.54
2	57–68	A1	0.23	4.7	33.68	600	1.44
	69–74	E1	0.42	3.7	14.79	240	3.34
	75–86	A1	0.23	4.7	33.68	600	1.44
	87	B	0.3	4	n/a	30	2.21
	88–91	E1	0.42	3.7	14.79	240	3.34
3	92–104	A2	0.19	5.3	37.98	780	1.05
	105–108	E2	0.32	3.7	14.79	120	2.54
	109–132	A3	0.14	5.7	40.85	1440	0.72

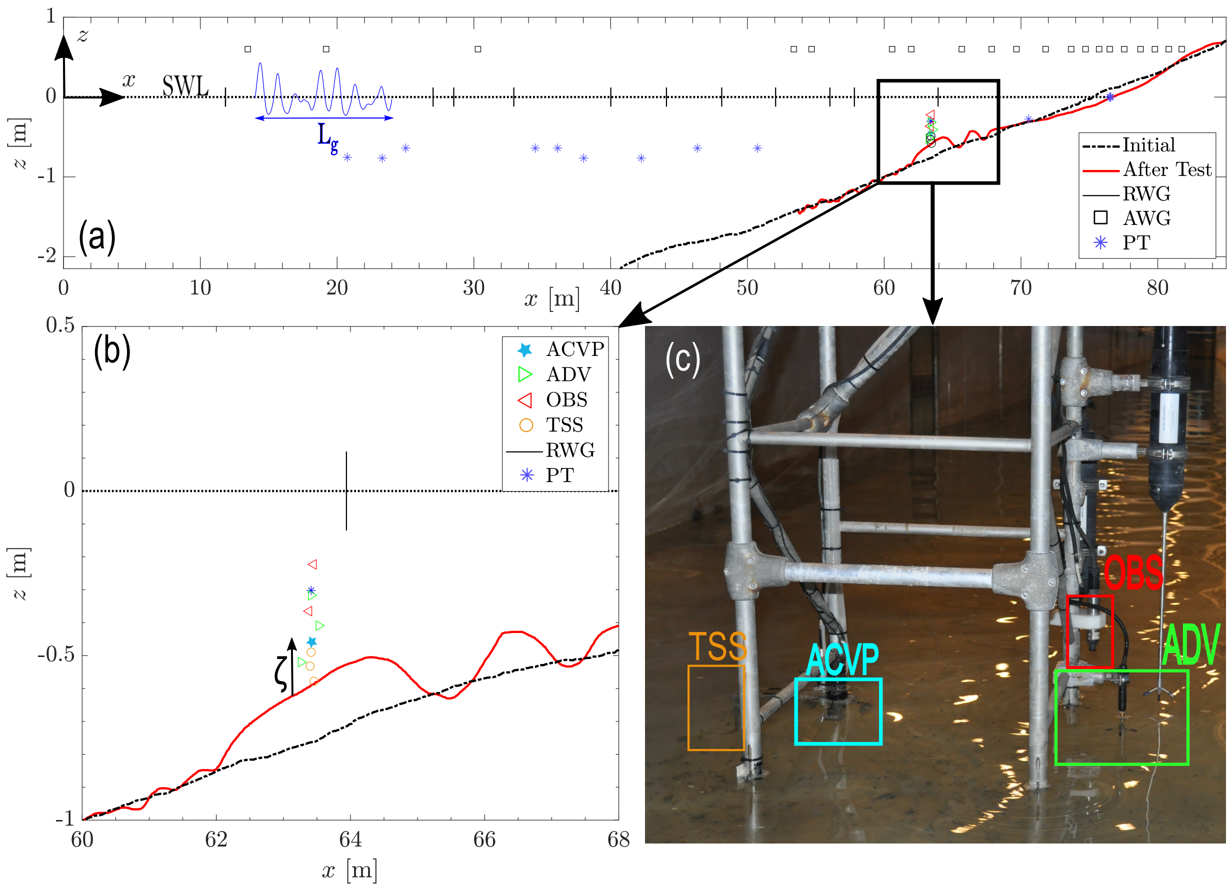

Figure 1. Layout of wave flume, experimental setup and instrumentation. (a) Entire wave flume with instruments and beach profile at the start of waves (black) and after 120 minutes of testing (red); (b) Schematic representation of instruments on mobile frame; (c) Photo of instruments on mobile frame; note that one OBS is located on the non-visible side of the frame.

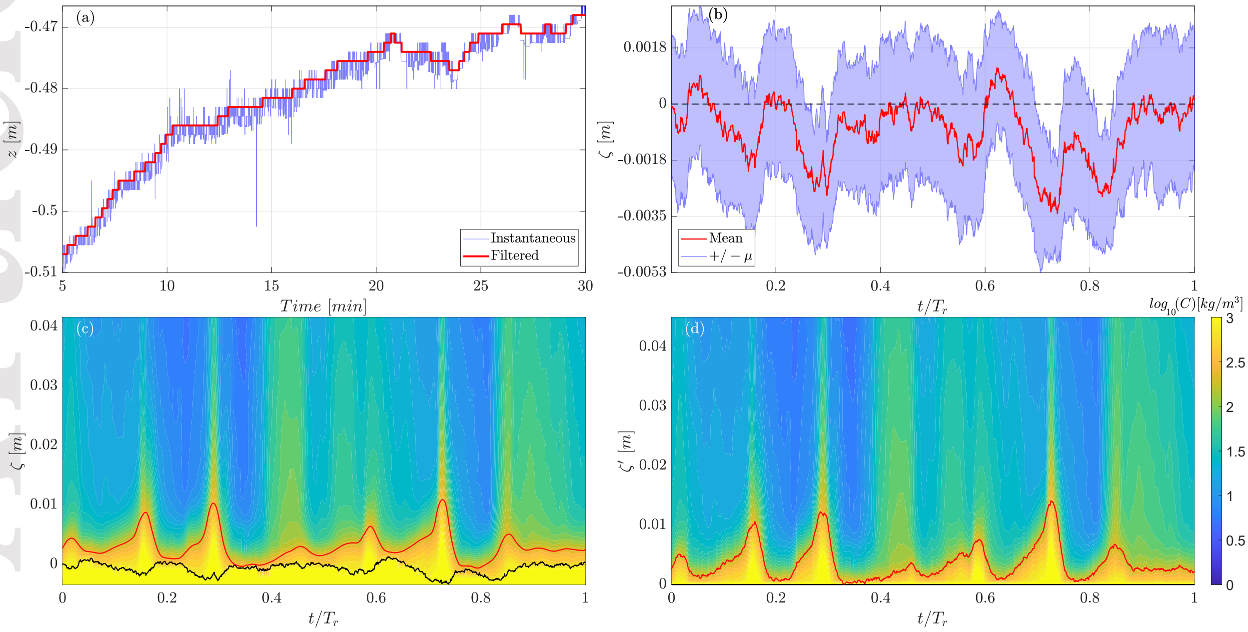

Figure 2. Differences in vertical coordinate systems, exemplified via test 54. (a) Measured and filtered bed evolution over the whole test. They are shown in the absolute flume coordinate z, which refers to SWL; (b) Ensemble-averaged intrawave bed evolution (including one standard deviation envelope) over T_r, which refers to the bed elevation during the velocity upcrossing of the first short wave in the group; (c) and (d) Near-bed intrawave concentration field with upper sheet flow limit (red line) shown in two different coordinate systems as explained in the accompanying text (section 3.5). The intrawave bed elevation (black line) in (c) corresponds to the red line in (b). In (d) the intrawave bed elevation is used for additional referencing of measurements so that its value is constantly 0.

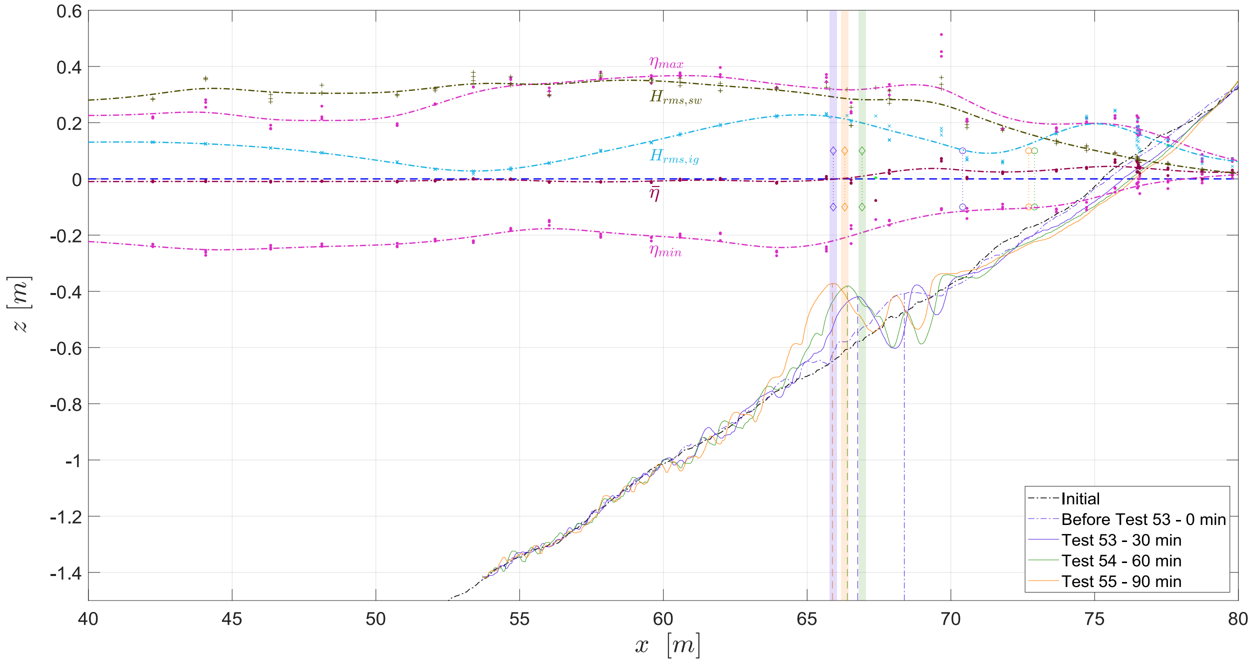

Figure 3. Example of profile evolution during application of benchmark (B) wave condition followed by three consecutive tests with erosive wave condition E2. SWL in dark blue dashed and profiles as indicated in legend (measured after the respective tests). Time-averaged water levels and short wave and infragravity wave wave heights with measured points plotted as markers and smoothing spline interpolation to obtain line. Visually observed outer breaking location (dashed vertical line with diamonds and transparent patch) and inner breaking location (dashed vertical line with circles). Identified bar maxima as dashed vertical lines.

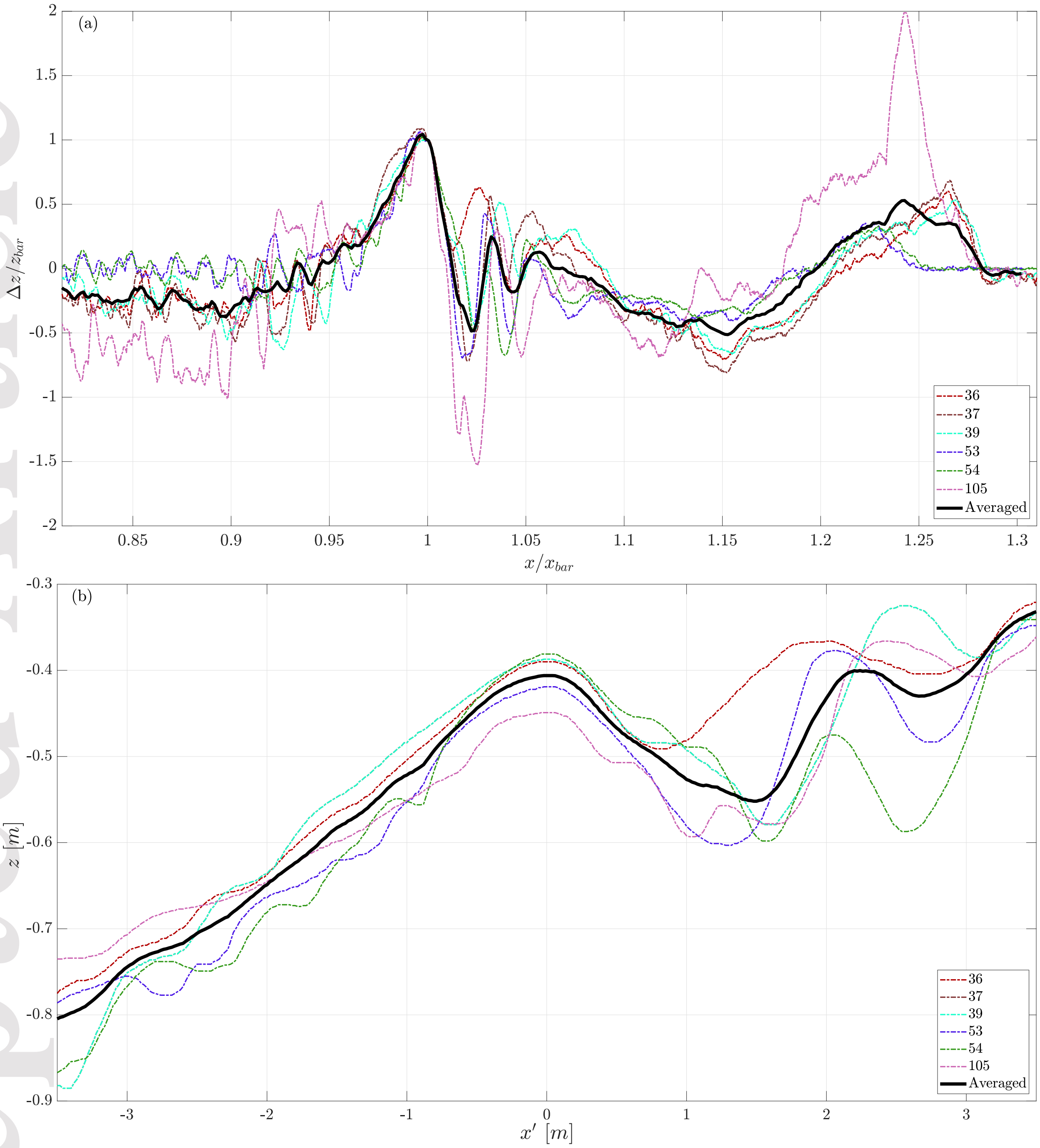

Figure 4. Generalization of morphological evolution in considered tests. (a) Bar coordinate-normalized bed evolutions (multiple colors) and their ensemble-average (black); (b) Beach profiles in vicinity of bar crest (multiple colors) and their ensemble-average (black). Note that $x/x_{bar} = 1$ in (a) refers to the same location as $x' = 0$ in (b).

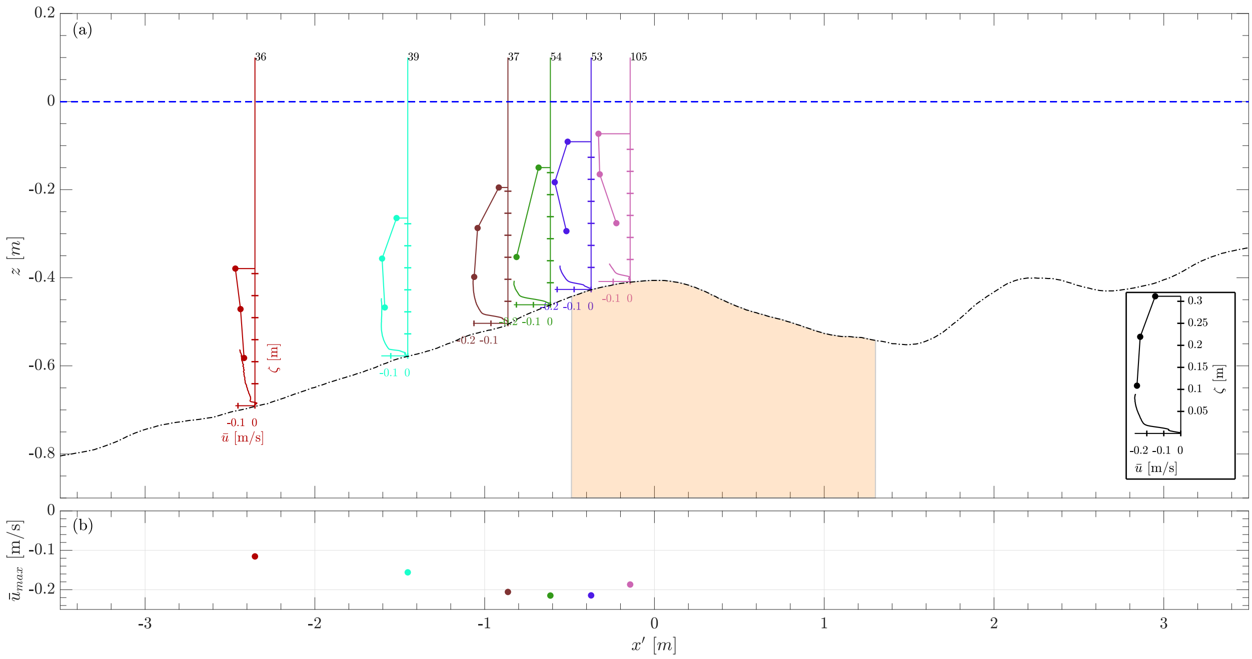

Figure 5. Time-averaged velocities in cross-shore positions relative to bar crest. (a) Horizontal velocity profiles from ACVP (near-bed solid lines) and ADVs (circles connected by solid lines) over ensemble-averaged beach profile (dashed-dotted black line) with SWL (dashed dark blue line) and test-averaged outer breaking location ± one standard deviation (shaded area); black sketch in the bottom right corner explains inset axes; (b) Maximum time-averaged, depth-dependent offshore velocity measured by ACVP and ADVs.

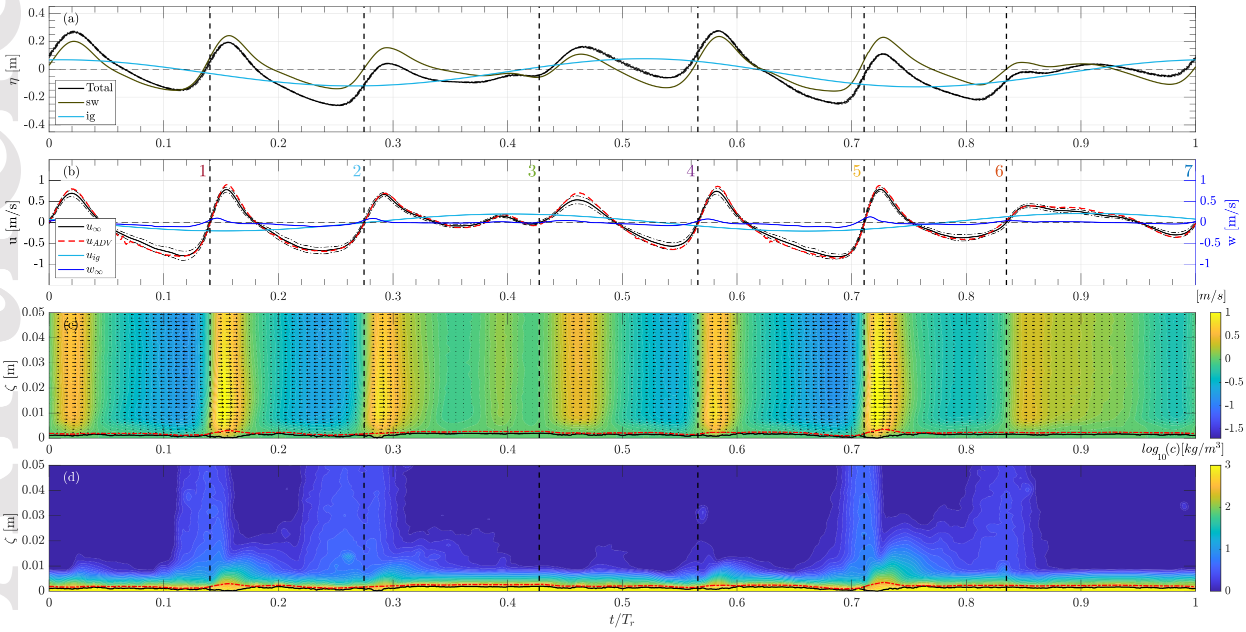

Figure 6. Hydrodynamic and sediment dynamics data in test 36 at 2.4m offshore of the bar crest in the shoaling region. Vertical dashed lines indicate separation into short waves, as numbered in (b). (a) Water surface elevations from PT shown before (black line with ± one standard deviation as black dashed-dotted line) and after separation into short wave (dark green) and infragravity contributions (light blue); (b) Free stream velocities from ACVP (featuring ± one standard deviation as black dashed-dotted line in u_∞) and lowest ADV, horizontal velocities referring to left y-axis and vertical velocity referring to right y-axis; (c) Near-bed velocity field from ACVP; (d) Near-bed concentration field from ACVP. Fields (c and d) referring to colorbars on their right and including instantaneous bed level (black) and upper limit of sheet flow layer (red dashed-dotted). Limited vertical extent of fields for focus on near-bed region.

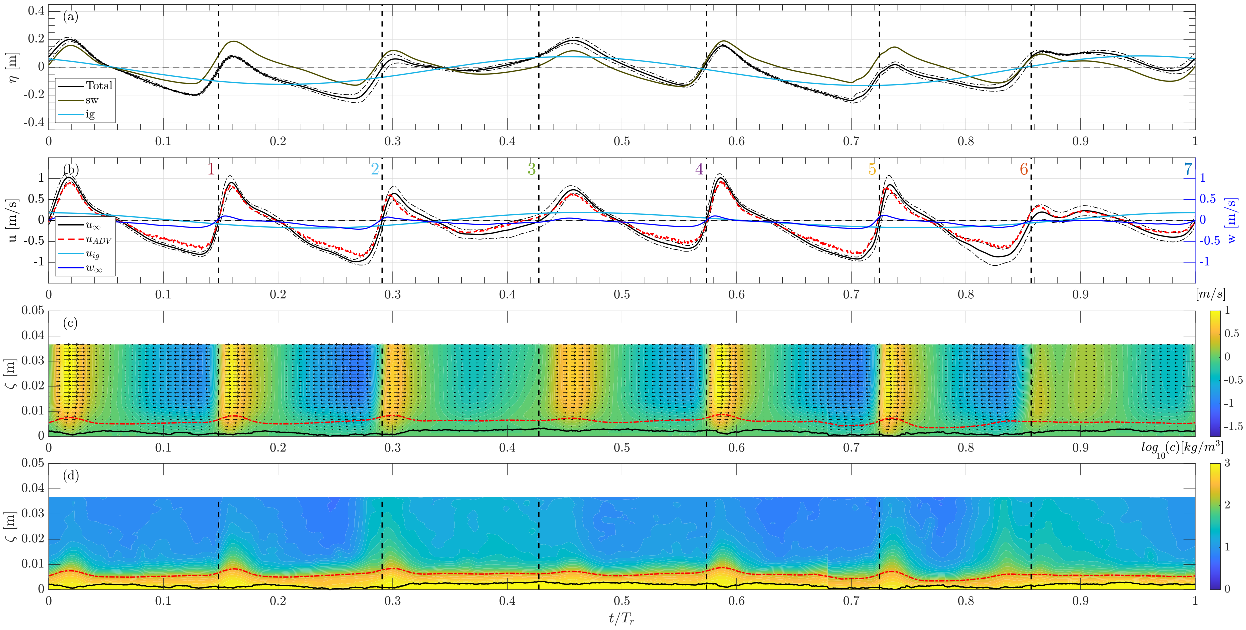

Figure 7. Hydrodynamic and sediment dynamics data in test 105 at 0.1m offshore of the bar crest in the outer breaking zone. Same definitions and color codes as previous figure. Discontinuity at $T_r = 0.685$ resulting from gateshifting on the basis of gradual bed erosion, as explained in detail in section 3.5.

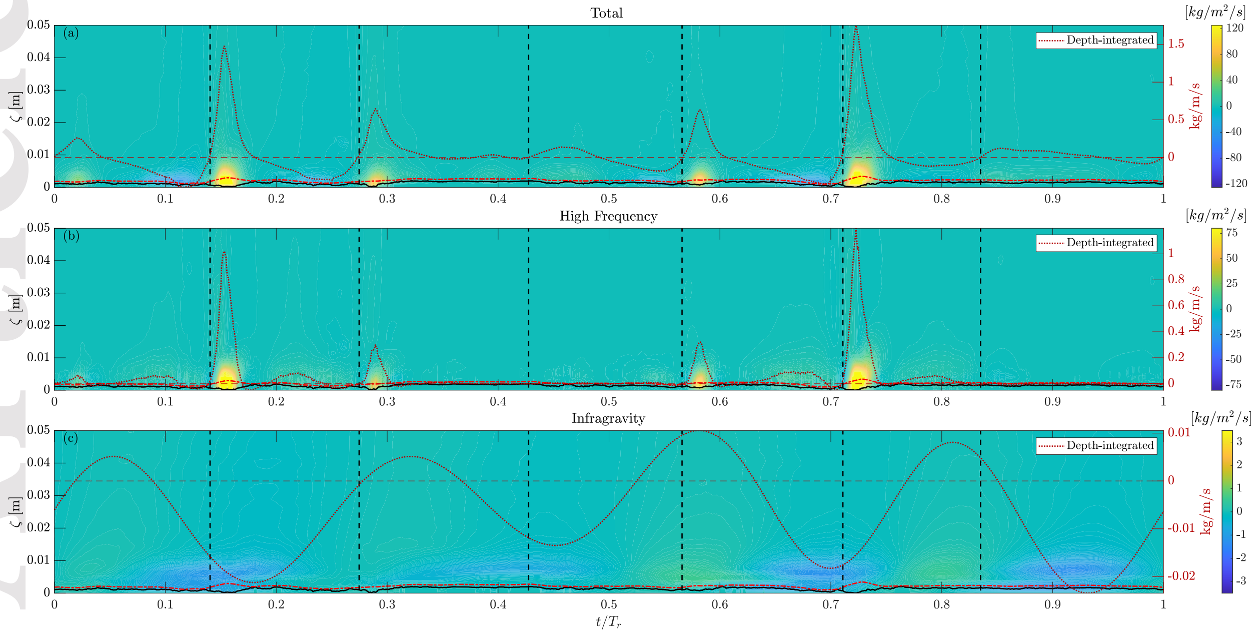

Figure 8. Decomposed sediment transport fields from ACVP with the depth-integrated transport rate (dotted line) combined from ACVP and OBS/ADV in test 36 at 2.4m offshore of the bar crest in the shoaling region. (a) Total, non-decomposed transport; (b) Short wave transport; (c) Infragravity transport. Note the different scales of the color contours and right y-axes. Instantaneous bed level (black solid line) and upper limit of the sheet flow layer (red dashed-dotted line). Furthermore, the shown onshore flux magnitudes in (a) and (b) were clipped at 125 and 80kg/m^2/s for representation purposes. The highest onshore transport magnitudes were 273 and 192kg/m^2/s, respectively in (a) and (b), and the limits were exceeded in 0.1% of the available data points (bright yellow patches). There is no intrawave time series for current-related transport rate but it amounted to -0.021kg/m/s.

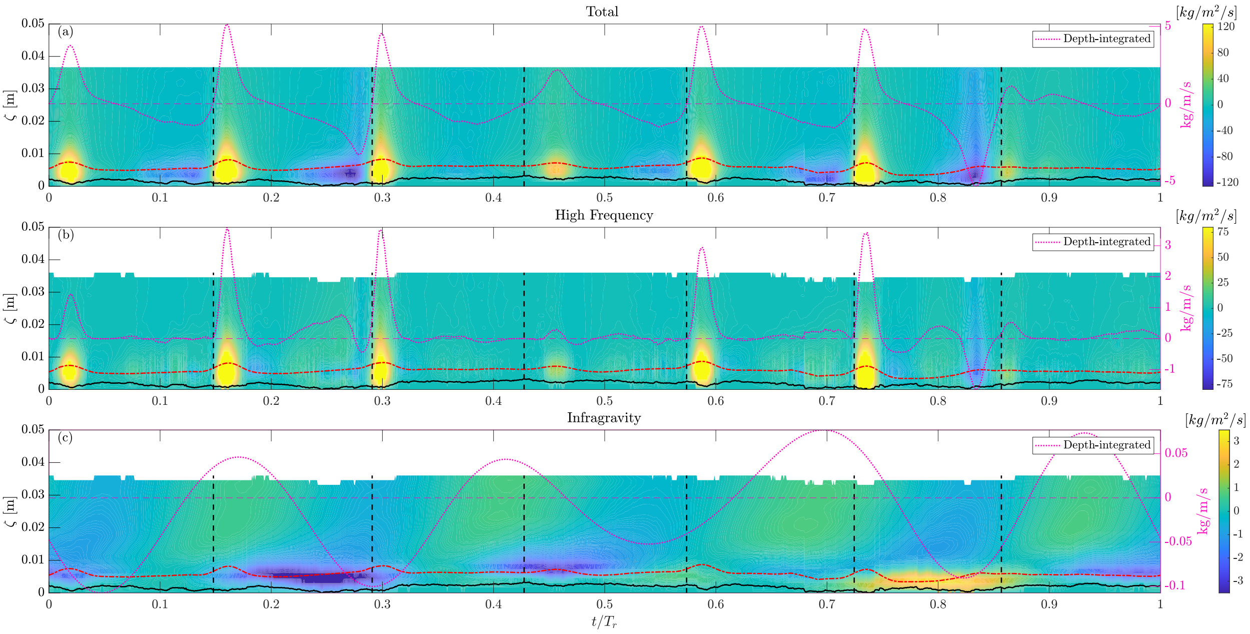

Figure 9. Decomposed sediment transport fields from ACVP with the depth-integrated transport (dotted line) combined from ACVP and OBS/ADV in test 105 at 0.1m offshore of the bar crest in the outer breaking zone. (a) Total, non-decomposed transport; (b) Short wave transport; (c) Infragravity transport. Note the different scales of the color contours and right y-axes. Instantaneous bed level (black solid line) and upper limit of the sheet flow layer (red dashed-dotted line). Again, the shown onshore flux magnitudes in (a) and (b) were clipped at 125 and 80kg/m^2/s for representation purposes. Here, the highest onshore transport magnitudes were 338 and 186kg/m^2/s, exceeding the limits in 1.5% and 1% of the available data points (bright yellow patches), respectively in (a) and (b). The chunky data gaps in (b) and (c) at $\zeta \approx$ 0.032m originate from the fact that calculations were conducted in the ζ'-coordinate system, as described in section 3.6. There is no intrawave time series for current-related transport rate but it amounted to -0.313kg/m/s.

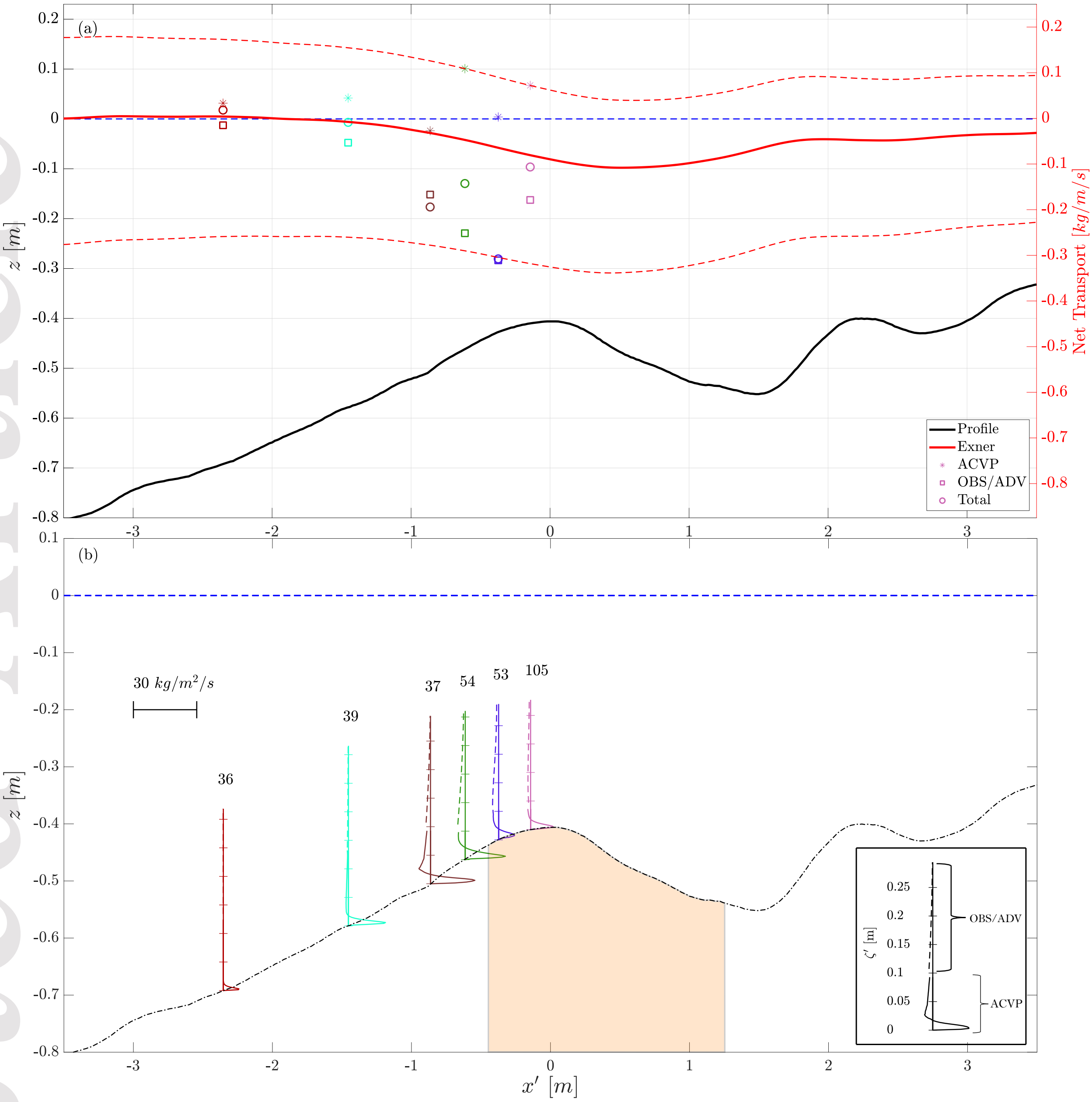

Figure 10. Net transport from mechanical profiler, ACVP and OBS/ADV. (a) Cross-shore evolution of net transport and comparison of net transport from the different methods. Profile transect measurements (red line referring to right y-axis) based on ensemble-averaging of Exner equation calculations in single tests with error bounds (red dashed lines) calculated as explained in accompanying text (section 4.5). ACVP and OBS/ADV measurements (markers of different shape with color indicating respective tests), on the other hand, are based on time-averaging and depth-integration of instantaneous measurements of horizontal velocity and sediment concentration in the ζ'-coordinate system. They are shown separately and as their summation ("Total"); (b) Net flux profiles from ACVP (solid lines) and OBS/ADV (dashed lines) in their respective cross-shore positions and test-averaged outer breaking location ± one standard deviation (shaded area).

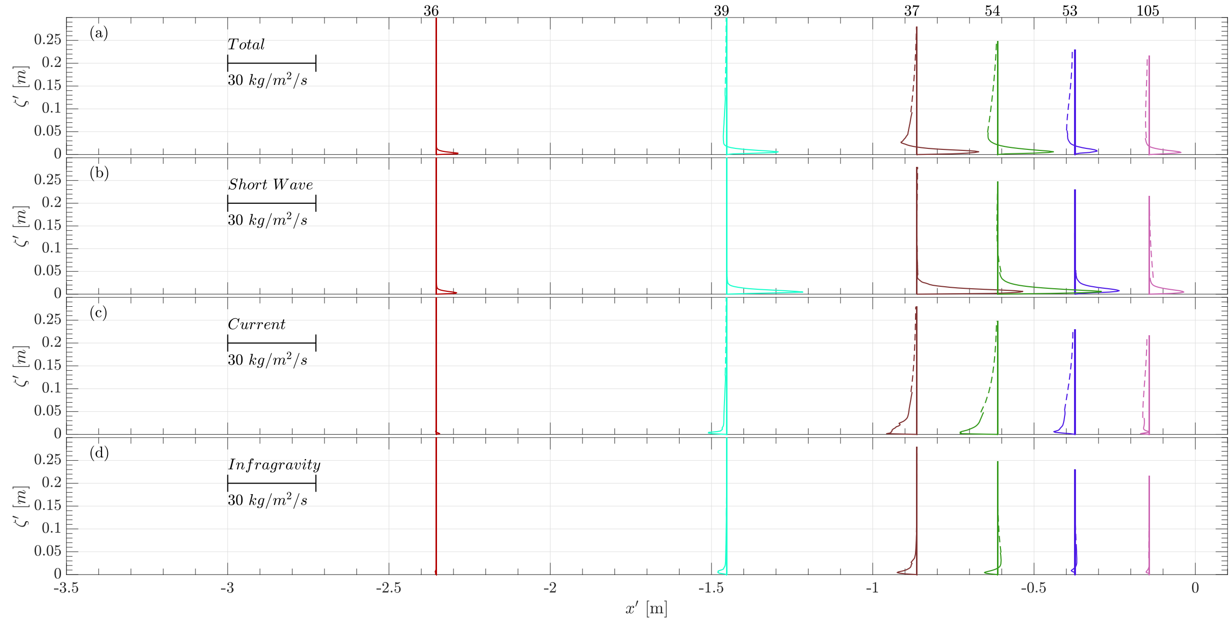

Figure 11. Decomposed net flux profiles (vertical extent of some profiles shortened for consistency) in their relative cross-shore positions. (a) Total; (b) Short wave component; (c) Current-related (mean) component; (d) Infragravity component. Combination of measurements from ACVP (solid line) and OBS/ADV (dashed line).

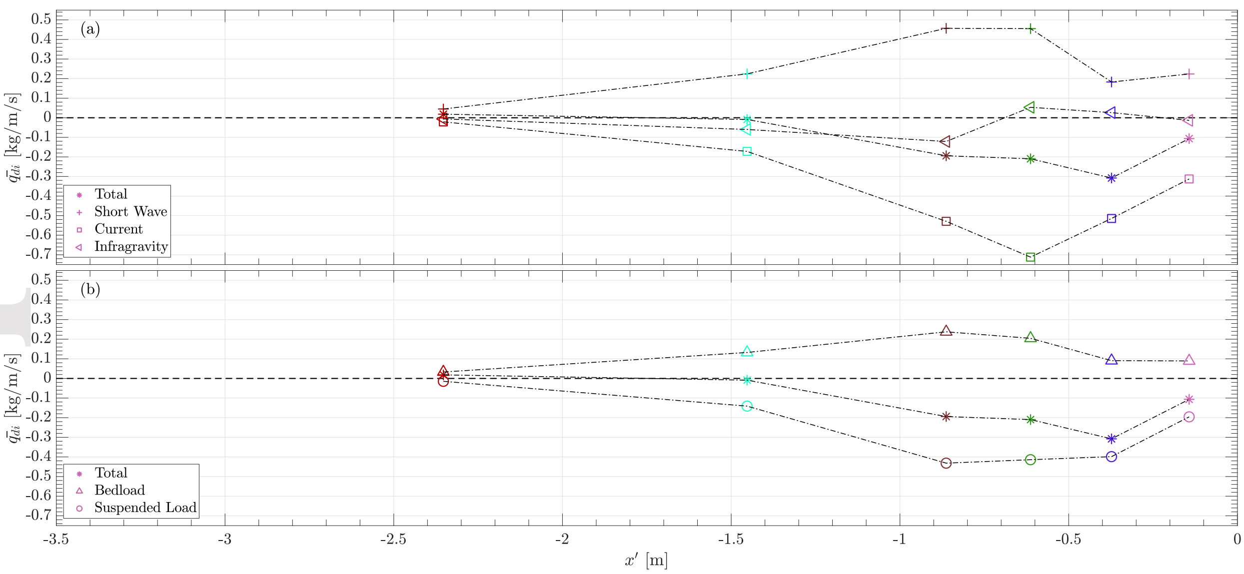

Figure 12. Depth-integrated (over entire available vertical extent as shown in Figure 10b), time-averaged sediment transports. (a) Frequency-decomposed; (b) Vertically-decomposed.

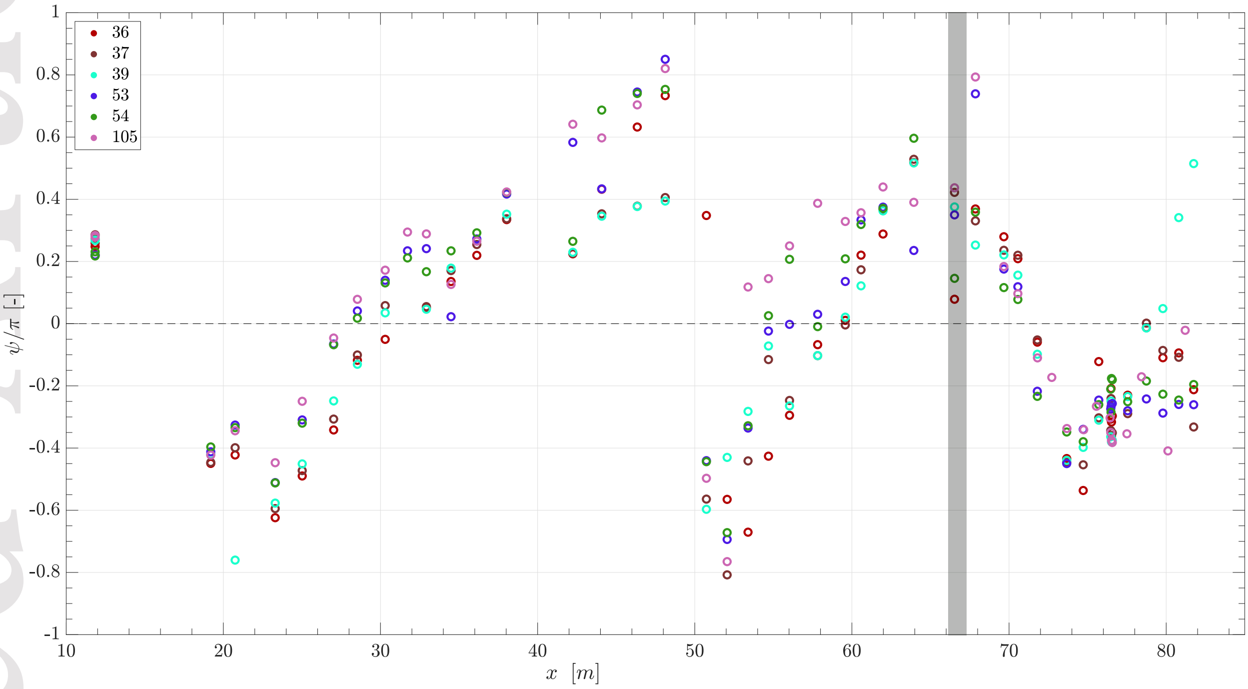

Figure 13. Phase lags ψ between infragravity waves and short wave envelopes (calculated from Hilbert transform). Different colors according to test number as shown in the legend. Horizontal axis referring to absolute cross-shore positions. Outer bar crest positions over all considered tests indicated by shaded area.